# Analysis of Lhù'ààn Mân' (Kluane Lake) dust plumes using passive and active ground-based remote sensing supported by physical surface measurements

Seyed Ali Sayedain[1], Norman T. O'Neill[1], James King[2], Patrick L. Hayes[2], Daniel Bellamy[2], Richard Washington[3], Sebastian Engelstaedter[3], Andy Vicente-Luis[2], Jill Bachelder[2], Malo Bernhard[2]

[1]Centre d'Applications et de Recherches en Télédétection, Université de Sherbrooke, Sherbrooke, Canada
[2]Université de Montréal, Montréal, Canada
[3]University of Oxford, Oxford, United Kingdom

*Correspondence to:* S. A. Sayedain (seyed.ali.sayedain@usherbrooke.ca)

**Abstract.** There is growing recognition that high latitude dust (HLD), originating from local, drainage-basin flows, is the dominant source for certain important phenomena such as particle deposition on snow / ice. The analysis of such local plumes (including a better exploitation of remote sensing data) has been targeted as a key aerosol issue by the HLD community. The sub-Arctic Lhù'ààn Mân' (Kluane Lake) region in the Canadian Yukon is subject to regular drainage, wind-induced dust plumes. This dust emission site is one of many current and potential proglacial dust sources in the Canadian North. In situ ground-based measurements are, due to constraints in accessing these types of regions, rare. Ground- and satellite-based remote sensing accordingly play an important role in helping characterize local dust sources in the Arctic and sub-Arctic.

We compared ground-based, passive and active remote sensing springtime (May 2019) retrievals with microphysical surface-based measurements in the Lhù'ààn Mân' region in order to better understand the potential for ground- and satellite-based remote sensing of HLD plumes. This included correlation analyzes between ground-based coarse mode (CM) aerosol optical depth (AOD) retrievals from AERONET AOD spectra, CM AODs derived from co-located Doppler lidar profiles and OPS (Optical Particle Sizer) surface measurements of CM particle-volume concentration ($v_c(0)$). An automated dust classification scheme was developed to objectively identify local dust events. The classification process helped distinguish lidar-derived CM AODs which co-varied with $v_{dust}(0)$ (during recognized dust events) and those that varied at the same columnar scale as AERONET-derived CM AOD (and thus could be remotely sensed). False positive cloud events for which dust-induced, high frequency variations in lidar-derived CM AODs in cloudless atmospheres indicated that the AERONET cloud-screening process was rejecting CM dust AODs. The persistence of a positive lidar ratio bias in comparing the CIMEL/lidar-derived value with a prescribed value obtained from OPS-derived particle sizes coupled with dust-speciation-derived refractive indices led to the suggestion that the prescribed value could be increased to optically-derived values of 20 sr by the presence of optically significant dust particles at an effective radius of 11–12 µm. Bimodal CM PSDs from full-fledged AERONET inversions (the combination of AOD spectra and almucantar radiances) also showed CM peaks at ~ 1.3 µm and 5–6.6 µm radius: this, we argued, was associated with springtime Asian dust and Lhù'ààn Mân' dust, respectively.

Correlations between the CIMEL-derived fine mode (FM) AOD and FM OPS-derived particle-volume concentration suggest that remote sensing techniques can be employed to monitor FM dust (which is arguably a better indicator of the long-distance transport of HLD).

## 1 Introduction

Local, drainage wind-induced dust events have recently been recognized as an important source of dust at high latitudes (Bullard et al., 2016). Groot-Zwaaftink et al. (2016) employed FLEXPART simulations to argue that the contributions of Asian, African, and local dust in the Arctic are roughly evenly divided in terms of total atmospheric (columnar) dust loads while surface concentrations are significantly more associated with dust of local origin. Meinander et al. (2022) employed two

40 global dust-transport models supported by recent verification data to confirm the predominance of high latitude dust (HLD) sources in terms of snow- and ice-deposition. This means, notably that, dust deposition on snow and ice and the attendant effects or early snow melt is largely attributable to local dust. Additional impacts of local dust deposition include direct addition of nutrients, local health impacts for humans & wildlife and indirect climate / radiative (altered cloud property) impacts (ibid.). These substantive impacts underscore the importance of understanding the dynamics of local dust transport and deposition.

45 Bullard et al. (2016) pointed out that local dust events in Canada are rarely monitored compared with other high-latitude countries. Low population density, limited numbers of meteorological stations, and problems with the use of satellite-based remote sensing (RS) data in high-latitude regions (e.g., cloud contamination) have led to less frequent observations of local dust events in Canada (ibid.). The next generation of active and passive polar-orbiting sensors targeted by the ESA EarthCARE mission and the NASA-led Atmospheric Observation System (AOS) promise a quality of aerosol, cloud and precipitation

50 retrievals that will make significant instrumental, algorithmic and scientific advances relative to the polar-orbiting A-train constellation (the workhorse remote sensing constellation that has driven atmospheric science over the past twenty two years). An intrinsic part of that system will be the ground-based Cal/Val sites that employ or will employ active and passive ground-based remote sensing sensors as well as microphysical measurements to monitor aerosols and clouds at existing and future sites across the Arctic. The Lhù'ààn Mân'[1] (Kluane Lake) region of Yukon, Canada will very likely be such a Cal/Val site in

55 the HLD context: it is recognized for its frequent and strong springtime dust events induced by strong katabatic winds, highly erodible sediments and the steep valley walls leading down to the lake (Bachelder et al., 2020).

The remote sensing of high latitude dust using active or passive ground-, airborne- or satellite-based platforms is rare. Some specific examples include the use of airborne (532 nm) lidar profiles to detect local dust plumes over riverbed, fjord and coastal regions of Svalbard (Dörnbrack et al., 2010), MODIS-based color and AOD (aerosol optical depth) imagery for dust

60 plumes emanating from Alaskan riverbed sediments into the Gulf of Alaska (Crusius et al., 2011), the investigations by

---

[1] Lhù'ààn Mân' is the Southern Tutchone name for Kluane Lake. Southern Tutchone is one of seven Athapaskan languages in the Yukon and is spoken by Kluane First Nation people.

Dagsson-Waldhauserova et al. (2019) who employed MODIS color imagery and attempted to use satellite-based CALIOP lidar profiles to support their airborne particle size distribution measurements of Icelandic dust plumes and MODIS, MISR, CloudSat / CALIOP optical depth and particle size characterization of local dust plumes over Lake Hazen in the high Canadian Arctic (Ranjbar et al., 2021). Ground-based data retrievals using solar extinction and sky radiometry data are widely used by

65    the AERONET (AErosol RObotic NETwork) to characterize the optical and microphysical properties of aerosols at local (site focused) scales (Holben et al., 1998). AOD and almucantar sky radiance measurements are carried out using the CIMEL sunphotometer / sky radiometer. Spectral Deconvolution Algorithm (SDA) retrievals can be employed to investigate high frequency event-level studies (O'Neill et al., 2003) while the more comprehensive AERONET inversion algorithm (Dubovik & King, 2000) can be employed for low frequency, climatological-scale analysis (see Hesaraki et al., 2017 for a more detailed

70    discussion). Publications on the use of AERONET retrievals to characterize the properties of local dust events at high latitudes are rare.

Huck et al. (2023) employed meteorological measurements, along with AERONET AODs and Angstrom exponents (AOD spectral information), a remote camera and satellite imagery to investigate dust event detection limits in the Lhù'ààn Mân' region. One notable conclusion was that the oblique camera captured many dust blowing incidents that were not being detected

75    by the CIMEL. Various explanations for this discrepancy were offered: these included the notion that Lhù'ààn Mân' plumes are very locally inhomogeneous and that wind direction could influence AERONET dust detection, that the CIMEL instrument missed plumes below its minimum angular elevation, that AERONET sensitivity was frequently too coarse to detect weaker events, that AERONET cloud screening removed 97.8% of dust events and that the CIMEL employed for the analysis (for which data acquisition occurred during the 2018 dust season) was incapable of making nighttime measurements.

80    Ground-based (and, even more so, satellite-based) remote sensing methods suffer from and benefit from their relatively coarse, column-based spatial scale and their minute to hourly to daily temporal scale. Columnar methods integrate the aerosol effects of the whole column and rely on other dimensions of information to separate out the optical influence of low altitude dust plumes. This same coarseness can have the tendency to produce robust dust signals if the dust plume scale is commensurate with the remote sensing scale. Another challenge related specifically to ground-based and specifically

85    AERONET retrievals is the excessively aggressive cloud screening that can screen out a dust event (Evan et al., 2021) and secondly, insufficiently aggressive cloud screening that leaves residual cloud OD to contaminate potential dust signals. Surface microphysical measurements such as PSDs and vertical profiling measurements such as lidar backscatter profiles can help to verify that a coarse mode (CM) is actually associated with a dust event.

We seek to employ ground-based, passive and active (lidar) RS techniques to analyze the complementarity and redundancy

90    of optical and microphysical retrievals relative to springtime CM measurements of local dust acquired using microphysical instruments at Lhù'ààn Mân'. The key ground-based instruments include a CIMEL sunphotometer / sky radiometer, a Doppler lidar operating in the SWIR (short-wave infrared), and an Optical Particle Sizer (OPS) for the measurement of near-surface particle-volume size distributions (PSDs). The coherencies and incoherencies between the passive AERONET retrievals and

near-surface PSDs, between AERONET CM AODs and the lidar backscatter profiles and their derived CM AODs (largely
95    generated by CM particle backscatter for the Doppler SWIR lidar) and between the lidar profiles and the CM portion of the
near-surface PSDs will enable a better understanding of the optical and microphysical properties of local dust plumes and will
help in improving ground-based and satellite-based remote sensing retrievals of local dust properties.

## 2 Research site and instrumentation

The Lhù'ààn Mân' region in the Canadian Yukon is subject to regular drainage-wind dust plumes emanating from the
100   Slims River basin (Nickling, 1978). The recent Kaskawulsh glacier retreat in the Slims River Valley and the river
reorganization event (Shugar et al., 2017) prompted the fall of water levels and the season-long exposure of the river delta and
floodplain. This caused extended periods of dust emissions induced by Aeolian erosion (ibid.). Typically, the period of the
most intense dust events is the spring and summer of each year (Bachelder et al., 2020).

The Kluane Lake Research Station (KLRS) is an established University of Calgary (Atmospheric Institute of North
105   America) site on the southern shore of Lhù'ààn Mân' (see Fig. 1). The AERONET CIMEL, Doppler lidar and OPS data
employed in this paper were acquired at KLRS during the month of May 2019. The May 2019 campaign was an intense part
of a continuous strategy to extract and analyze Lhù'ààn Mân' dust plume properties using a suite of optical, microphysical,
and meteorological instruments (ibid.).

Details on the CIMEL sunphotometer / sky radiometer and associated processing protocols can be found in Giles et al.
110   (2019). AEROCAN, the Canadian subnetwork of AERONET (maintained by Environment and Climate Change Canada)
provides direct instrument troubleshooting and swapping out support for all Canadian AERONET sites. This instrument
provides spectral AOD retrievals at a nominal high frequency of one (9-band) AOD spectrum per 3 minutes (9 bands from 340
to 1640 nm[2]). It also provides a comprehensive suite of low frequency (nominally once per hour) microphysical and optical
retrievals derived from almucantar radiance scans and 4-band AODs.

115   The high frequency (11-second time bin) Doppler (HALO Photonics) lidar (Pearson et al., 2009) was averaged to the 1-
minute CIMEL time bins. The vertical resolution of the lidar is 3 m based on 30 m overlapping gates with a typical range of <
LCH (Lidar Ceiling Height which is equal to 9.6 km; Newsom & Krishnamurthy, 2020). Its 1.5 µm wavelength (more precisely
1.548 µm according to ibid.) is largely the result of a strategical decision to minimize molecular contributions to the backscatter
signal (see, ibid., for example). The FM AOD at the lidar wavelength is typically negligible (see below).

120   The KLRS surface-PSD device is a TSI Optical Particle Sizer (OPS) 3330 instrument that incorporates 16 size bins with
bin-center radii extending from 0.17 to 4.51 µm (bin-center diameters from 0.34 to 9.02 µm). Two supporting FAI Optical

---

[2] Including two bands at 1020 nm that are associated with the overlap region of the two CIMEL detectors (the VIS–NIR and
NIR–SWIR detectors).

Particle Counter (OPC) instruments provided analogous PSD measurements[3] at the Down Valley (DV) site about 7 km southwest of KLRS (see Fig. 1 for the DV position and Bachelder et al., 2020 for details on the OPC instruments). The KLRS OPS and the two DV OPC instruments often provided important redundancy information (as well as insightful information 125 stemming from their differences) when we sought to investigate the presence and nature of a given CM event.

A dust event captured in a 27 May 2019 PlanetScope satellite image acquired over Lhù'ààn Mân' is shown in Fig. 1 (the KLRS and DV site positions are indicated by red and green stars respectively). AERONET CM AOD retrievals are represented by the blue-colored profile in the bottom right-hand corner of the image. The time of the PlanetScope image acquisition is indicated by the arrow on the AERONET plot. The sun-pointing CIMEL instrument was looking southeast at the time of the 130 PlanetScope image acquisition while dust plumes can be seen flowing from the whitish Slims River basin and delta. The blue-colored AERONET CM AOD shows quite large values during the period (late morning to early afternoon) when the optically significant dust plume intercepts the CIMEL line of sight (from the roughly eastern to western directions).
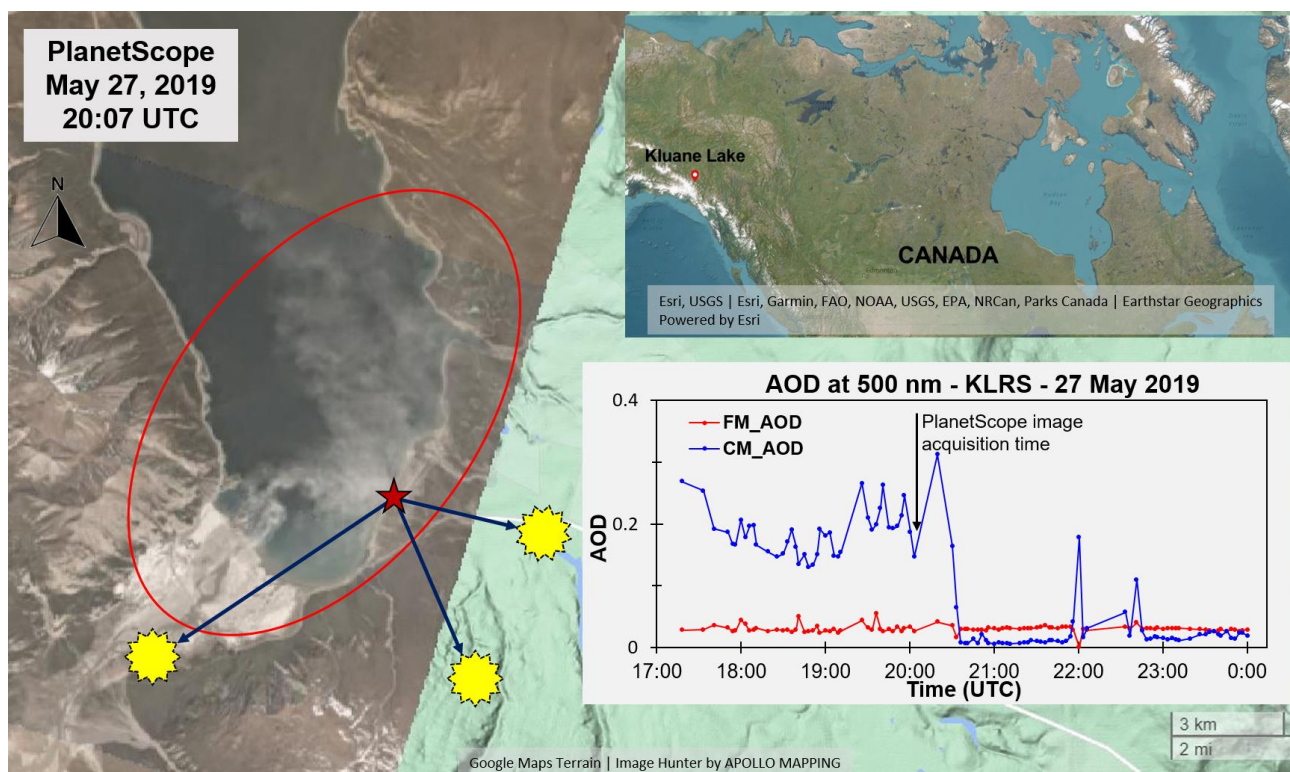
Figure 1: Lhù'ààn Mân' (Kluane Lake) study area as seen in a 27 May 2019 PlanetScope satellite image (ESA/NASA). A dust plume can 135 be seen emanating from the whitish Slims River basin. The KLRS and DV site positions are indicated by the red and green star respectively. The CM AOD and FM AOD time series in the bottom right-hand corner is a standard (SDA) AERONET Version 3, Level 1.0 (500 nm) product (the CM AOD at the lidar wavelength of 1.548 µm will only change by a moderate amount relative to the 500 nm value). The solar-

---

[3] across 22 size bins whose bin-center radii extend from 0.14 to 5.0 µm (bin-center diameters from 0.28 to 10 µm)

viewing azimuth direction of the CIMEL is shown yellow solar icons (clockwise from 17:00 UTC at the upper right to 20:07 UTC to 00:00 UTC on May 28). The coordinates of the AERONET / AEROCAN station are 61.027° N, 138.41° W.

## 3 Methodology

### 3.1 AERONET processing

We employed Version 3.0 Level 1.0 AODs and Level 1.5 AERONET inversions to extract retrieval products that could be compared with the lidar and the KLRS OPS data sets (see Giles et al., 2019 for an overview of Version 3.0 AERONET AOD products and Sinyuk et al., 2020 for an overview of Version 3 AERONET inversions). The algorithm used for comparisons with the Doppler lidar data was the high frequency (nominally 1 minute averaging bin, 3 minute intersample gap) SDA$^+$ product extrapolated to the Doppler SWIR wavelength of 1.548 µm (see O'Neill et al., 2008 for a discussion of the SDA$^+$ algorithm). We label this ARONET-derived CM AODs as $\tau_c$.

The low frequency (nominally 1-hour intersample gap) AERONET inversion products (Dubovik & King, 2000) include the particle-volume PSD per unit increment in logr ($dV/dlnr$) over 22 radius bin centers (stretching from 0.05 to 15 µm) along with pan-PSD refractive index, scattering phase function and associated optical products such as the asymmetry factor across four spectral bands (440, 675, 870, and 1020 nm). These fundamental products are accompanied by derived products of CM and FM particle-volume concentration and effective radius as well as CM and FM AODs across the same four spectral bands.

An important intensive (per particle) AERONET inversion product is the (column averaged) CM effective radius (see Hansen & Travis, 1974 for a definition of the effective radius and AboEl-Fetouh et al., 2020 for a discussion of the FM and CM AERONET-inversion effective radius product). In the absence of clouds and in the presence of a strong columnar dust activity, this parameter may provide an important and robust indicator of column-averaged effective radius. The same can be said of the refractive index product with two notable riders: the pan-PSD nature of the product can become problematic in the presence of an (optically) competitive FM aerosol of distinctly different refractive index and the rapidly increasing refractive index and single scattering albedo retrieval errors (notably for desert dust) with decreasing AOD (Sinyuk et al., 2020).

### 3.2 Lidar processing

Basic lidar definitions are given, for example, in Weitkamp (2005). The essential quantities that we require in order to transform the Doppler lidar profiles into CM extinction coefficient and lidar-derived CM optical depth ($\tau_c^\ell$) are the CM backscatter coefficient ($\beta_c$) and the CM lidar ratio ($S_c$). The actual lidar outputs are $\beta'(z) = \beta(z)\, T^2(z)$ (attenuated backscatter coefficient) profiles where $T^2(z)$ is the altitude (z) dependent return (two-way) transmission of a lidar pulse from the ground (z = 0). Optical depths for submicron particles at the lidar SWIR wavelength are negligible (we already know that

to be true for molecular scattering and it is generally a good approximation if dust optical depths are >~ 0.1: see, for example, Fig. 2 of O'Neill et al., 2008[4]).

If we apply this CM dominance to the $\beta'(z)$ and $\beta(z)$ profiles then;

$$\beta'(z) \cong \beta_c'(z) = \beta_c(z) \, T_c^2(z) \tag{1a}$$

170    The two-way transmission can be approximated by;

$$T_{c,\sim}^2(z) \cong exp\left[-2\,\tau_c\left(\tau_{\beta_c'}(0,z)/\tau_{\beta_c'}\right)\right] \tag{1b}$$

where $\tau_c$ is a CIMEL-derived value at the lidar wavelength ($\tau_c$ values interpolated to the nominal time of a given lidar profile) and $\tau_{\beta_c'}(0,z)/\tau_{\beta_c'}$ amounts to a dynamic approximation of $\tau_c(0,z)/\tau_c$ for that profile (the reader will note that, for the sake of nomenclature simplicity, we only employ the partial column argument "$(0,z)$" when it helps to underscore an explicit

175    point). We can then approximate $\beta_c(z)$ by:

$$\beta_{c,\sim}(z) \cong \beta_c'(z)/T_{c,\sim}^2(z) \cong \beta_c(z) \, T^2(z)/T_{c,\sim}^2(z) \tag{2}$$

The division by $T_{c,\sim}^2(z)$ means (whether it is an approximation or not) that the derived $\beta_c(z)$ values will appear progressively brighter than $\beta_c'(z)$ values as z increases with an attendant potential for error as $T^2(z)$ and $T_{c,\sim}^2(z)$ become very small. However, the $T_{c,\sim}^2(z)$ values are increasingly piniored (in addition to the near-surface restraint of near unity

180    transmission) by the CIMEL-estimated true value ($exp[-2\,\tau_c]$) as z increases towards the upper extreme of the $\beta_c'(z)$ integration (top of a dust plume in the case of a clear-sky dust event).

### 3.2.1 Prescribed lidar ratio for dust

A prescribed KLRS-derived lidar ratio[5] for dust ($S_c^p$; results presented below) and a prescribed lidar ratio for cloud (Chiang et al., 2002) were employed to calculate $\tau_c^\ell$ for dust and cloud. If $\tau_{\beta_c}$ is defined as $\int \beta_{c,\sim}(z)\,dz$ then;

185    $$\tau_c^\ell \cong S_c^p \tau_{\beta_c} \tag{3}$$

$S_c^p$ can be computed from a priori or measurement information on refractive index, particle size and particle shape. We discuss below (Sect. 4.3.1.2) how the prescribed KLRS-derived $S_c^p$ value for dust was arrived at and how much uncertainty was associated with that value.

---

[4] For FM AODs of <~ 0.4 at 500 nm (a maximum FM AOD of 0.4 is generally greater than any values that could be found, in the absence of the easily detectible influence of biomass burning smoke, at Lhù'ààn Mân'). During the month of May 2019 there were FM AOD events on May 7/8 and May 24 (associated, it would appear with CM dust events) for which the 500 nm FM AOD for the former case was as large as ~ 0.2).

[5] To be clear about the definition of lidar ratio, we note that its general definition is $1/[\omega_0\,p(\pi)]$ (with a Rayleigh / molecular value of $8\pi/3$) and that $\omega_0$ and $p(\pi)$ are respectively, the single scattering albedo and scattering phase function at a scattering angle of $\pi$ radians and where the integration of $p(\chi)/[4\pi]$ over $4\pi$ steradians is unity.

### 3.2.2 Validation of prescribed lidar ratio

190    CIMEL values of $\tau_c$ were employed to validate the prescribed dust lidar ratio (effectively the replacement of $\tau_c^\ell$ by $\tau_c$ in Eq. (3) above). Details of the validation parameterization are given in Appendix A1. The process explicitly incorporates $S_c^p$ and $\tau_c^\ell$ and CIMEL-derived $\tau_c$ values to compute a CIMEL-referenced lidar ratio ($S_c$). It includes an accounting of the day-to-day correlations between $\tau_c^\ell$ and $\tau_c$ (which may or may not be strong during any given period of interest) and how those correlation results should be weighted.

### 3.3 OPS and OPC processing

195

    The KLRS OPS and the DV OPC PSD measurements of $dn/dlogD$ (particle number / unit volume of air / unit increment in logarithmic diameter) were converted to $dv/dlogD$ (particle-volume / unit volume of air / unit increment in logarithmic diameter) assuming spherical particles[6]. We integrated the OPS PSDs over the CM radius range (bin-centers of 0.78 to 4.51 µm) to yield the CM particle-volume concentration ($v_c(0)$: the volume of all CM particles per unit volume of air). The near-

200    surface OPS and OPC particle-volume PSDs ($\frac{dv}{dlogr} = \frac{4}{3} \pi r^3 \frac{dn}{dlogr} = \frac{4}{3} \pi r^3 \frac{dn}{dlogD}$) are analogous to the columnar particle-volume PSDs ($dV/dlnr$) products of the AERONET inversion (columnar particle-volume per unit area) while the $v_c(0)$ parameter is analogous to the AERONET CM-integrated particle-volume density ("VolC-C" or $V_c$) product. Since we only consider events that are likely to be dust events (as evidenced by the lidar-measured presence of a dust plume) we will generally label $v_c(0)$ as $v_{dust}(0)$.

### 3.4 Correlation analysis

205

    Indicators of the optical significance and remote sensing detectability of a dust event can, we would argue, be represented respectively by how dust-related $\tau_c^\ell$ correlates with the KLRS OPS measurements of $v_{dust}(0)$ and how well $\tau_c$ correlates with dust-related $\tau_c^\ell$. Our dust (and cloud) classification methodology defined below is largely based on the coefficient of correlation between $v_{dust}(0)$, $\tau_c^\ell$ and $\tau_c$.

210    Results such as those of Hesaraki et al. (2017) empirically indicate that geometric statistics of AODs (histograms and statistics computed in log-AOD space) are more representative than the arithmetic statistics of linear-AOD space and that a consequence of this is that $R$ values should be larger (results that will, however, always be subject to the vagaries of low-sample or "low-N" statistics). In order to better understand the degree of coherency between the three different types of data, we analyzed their correlations in linear-AOD and log-AOD space as a function of different time-bin amplitudes (results are

215    presented below).

---

[6] or more precisely, the radii of spherical particles that would be optically equivalent to irregularly shaped particles

### 3.5 Event classification

The classification methodology must clearly separate the optical effects of dust and clouds: the first step in this process is to isolate apparent dust plumes in the vertical profiles of the lidar. The dynamic process for arriving at a variable dust layer height (DLH) from the $\beta_{c,\sim}$ profiles is outlined in the Supplementary material (S2). An estimate of lidar-derived dust optical

220 depth ($\tau_{dust}^{\ell}$) can then be computed by vertical integrations of the $\beta_{c,\sim}$ profiles from the surface to the DLH. We then argue that $\tau_{cloud}^{\ell}$ values (or at least the CM optical depth of anything but local dust) are obtained by vertically integrating the $\beta_{c,\sim}$ profiles from the DLH to LCH.

We focused on two levels of correlation: the use of $R_{log}\left(\tau_{dust}^{\ell} \text{ vs } v_{dust}(0)\right)$ values as a means identifying and characterizing optically significant dust events and $R_{log}\left(\tau_c \text{ vs } \tau_{dust}^{\ell}\right)$ values to identify those events that could be remotely

225 sensed by a passive ground- or satellite-based instrument[7]. In the latter case the high frequency $\tau_{dust}^{\ell}$ values must be resampled to match the 1 minute time bins (3 minute intersample times) of the low frequency $\tau_c$ values: this process is described in Appendix A3. Our justification for the use of such a dust event flagging protocol is that correlation is a necessary (if insufficient) indicator of the presence of a dust event and that it is largely impervious to systematic instrumental issues (calibration issues for example). Verification of correlation-based dust event flagging is usually supported (contextualized) by

230 other types of indicators (the recording of strong basin winds, for example). We attributed the following event-classification codes for different, event-level periods of interest (POIs).

#### 3.5.1 Optically significant (*D* class) dust

Our fundamental classification is that of a dust (*D*) class that appears to be optically significant at the columnar optical depth scale. A POI was defined as belonging to the *D* class if:

235
$$R_{log}\left(\tau_{dust}^{\ell} \text{ vs } v_{dust}(0)\right) \geq 0.5$$

This class basically requires that local KLRS OPS variations at the surface be at the same scale of variation as the columnar lidar optical depths (i.e. something that would not likely be true for dust turbulence scales ~ a few meters).

#### 3.5.2 Optically insignificant (*U* class) dust

We labelled a POI that failed to satisfy the *D* class criterion as a U (unknown) event (this includes cases for which there

240 were less than 10 matched OPS-lidar matched samples):

$$R_{log}\left(\tau_{dust}^{\ell} \text{ vs } v_{dust}(0)\right) < 0.5$$

---

[7] The latter correlation is complicated by AERONET cloud screening protocols: potentially strong dust-induced correlations might, for example be inadvertently eliminated by the Level 1.0 triplet processing or the Level 1.5 cloud screening process.

### 3.5.3 *D* and *U* subclasses

The *D* classification rule leads to two subclass children: class *D* events that can and cannot be remotely sensed (respectively $D_{RS}$ and $D_{NRS}$). In the former case we would argue that the potential for achieving the satellite-based remote sensing of a dust

245 event must require that a passive ground-based measurement of a candidate dust plume ($\tau_c$) must be significantly correlated with its lidar analogue. The $D_{RS}$ subclass was accordingly defined as:

$$R_{log}\left(\tau_c \; vs \; \tau_D^\ell\right) \geq 0.5$$

This means that the correlation must be roughly impervious to spatio-temporal sampling differences between the lidar and the photometric measure (including the fact that the photometric measure represents a completely different line of sight relative

250 to zenith looking lidar). The complementary $D_{NRS}$ subclass follows as:

$$R_{log}\left(\tau_c \; vs \; \tau_D^\ell\right) < 0.5$$

It includes, by default, cases for which there were less than $N(\tau_c) = 10$ retrievals or for which the lidar indicates the presence of cloud ($\tau_{cloud}^\ell \geq 0.001$)[8]. The *D* subclasses have their *U* subclass analogues: class *U* events that can and cannot be remotely sensed (respectively $U_{RS}$ and $U_{NRS}$):

255
$$R_{log}\left(\tau_c \; vs \; \tau_U^\ell\right) \geq 0.5$$
$$R_{log}\left(\tau_c \; vs \; \tau_U^\ell\right) < 0.5$$

The $U_{RS}$ subclass represents cases where the correlation between $\tau_c$ and $\tau_{dust}^\ell$ indicates the presence of a detectable remote sensing event of an unknown nature ("unknown" at least in the context of a "*D*" classification that is tied to threshold values of $R_{log}\left(\tau_{dust}^\ell \; vs \; v_{dust}(0)\right)$). The $U_{NRS}$ subclass represents a non-event that defies both a dust and a remote sensing label.

260 Figure 2 summarizes the dust classification paradigm in a more heuristic flowchart manner. For the sake of simplicity, the special $D_{FPC}$ and $D_{GEN}$ subclasses defined immediately below have been omitted from the flow-chart.

### 3.5.3 Special classes

A special false positive cloud subclass ($D_{FPC}$) was defined for which the AERONET cloud screening process appeared to eliminate real optical depth variations induced by a dust event: class *D* events for which $N(\tau_c) \leq 10$ and for which $\tau_{cloud}^\ell$

265 indicates no cloud. A special "generic" dust subclass ($D_{GEN}$) was defined to include events that were identified, with a reasonable certainty using circumstantial evidence. The circumstantial evidence could include combinations of, for example, lidar profiles, reports from measuring teams on the ground, RGB satellite images that visually show dust plumes over Lhù'ààn Mân' (the PlanetScope image of Fig. 1 for example), information from auxiliary measurements such as downslope wind velocity or PM10 devices, etc.

---

[8] the 0.001 minimum is an order of magnitude estimate of $\tau_c$ sensitivity to real physical CM changes (an estimate based on experiential evidence such as the seasonal variations observed by AboEl-Fetouh et al., 2020)
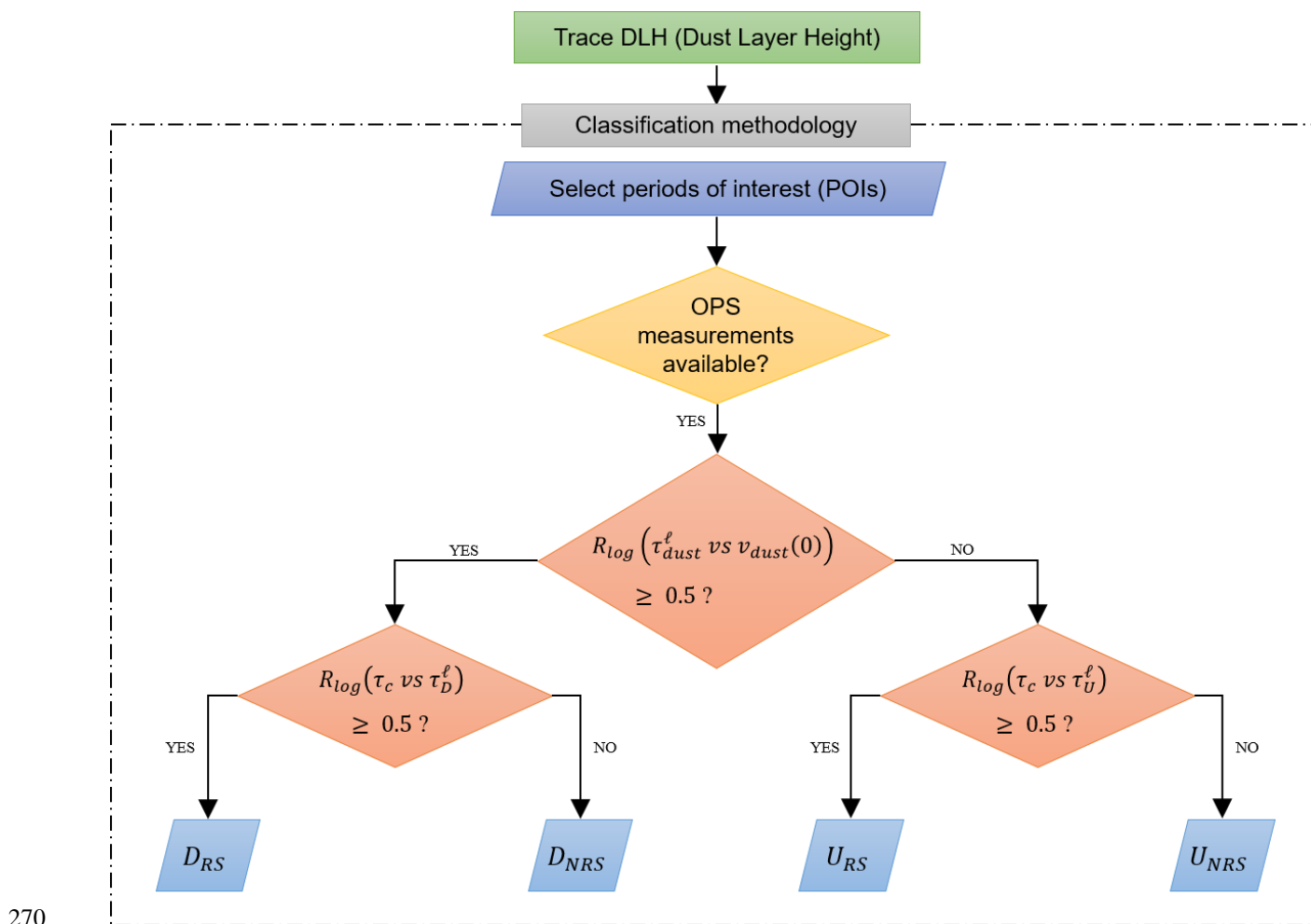
Figure 2: Flow-chart of the classification methodology described in the text. The different class symbols are defined directly above the flow chart. The $N(\tau_c)$ threshold is 10 samples. The $D_{FPC}$ and $D_{GEN}$ subclasses would be supplementary branches (not shown) from the "No" of the upper-level $R_{log}\left(\tau_{dust}^\ell \ vs \ v_{dust}(0)\right) \geq 0.5$ decision diamond.

## 4 Results

### 4.1 Lidar measurement overview

Figure 3 shows an overview of a $\beta_c(z)$ profile[9] over a time period in May of 2019 that includes a number of interesting events. Our intent here is (i) to illustrate the profile attributes (notably the logarithmic color legend) during a diversity of events as well as the fact that dust plume heights were generally less than 2 km (red-dashed line) and (ii) to give the reader an event

---

[9] Actually the profile is that of the $\beta_{c,\sim}(z)$ parameter of Eq. (2): we dropped the "~" subscript in our profile figures for the sake of simplicity.

continuity perspective that is not very evident in the (POI-driven) daily profiles found in the Supplementary material (S6). One

280   can observe a relatively strong and higher-altitude plume before the end of the daylight hours of May 7 (~ 03/08 UT) whose height appears to decrease in altitude and optical impact up to ~ 00/09 UT (followed by a strong but very low-altitude plume). Cloud formation can be observed between about 5 and 8 km altitude) during the nighttime (white-night) period (sun below 10° elevation from about 03/08 to 13/08 UT).
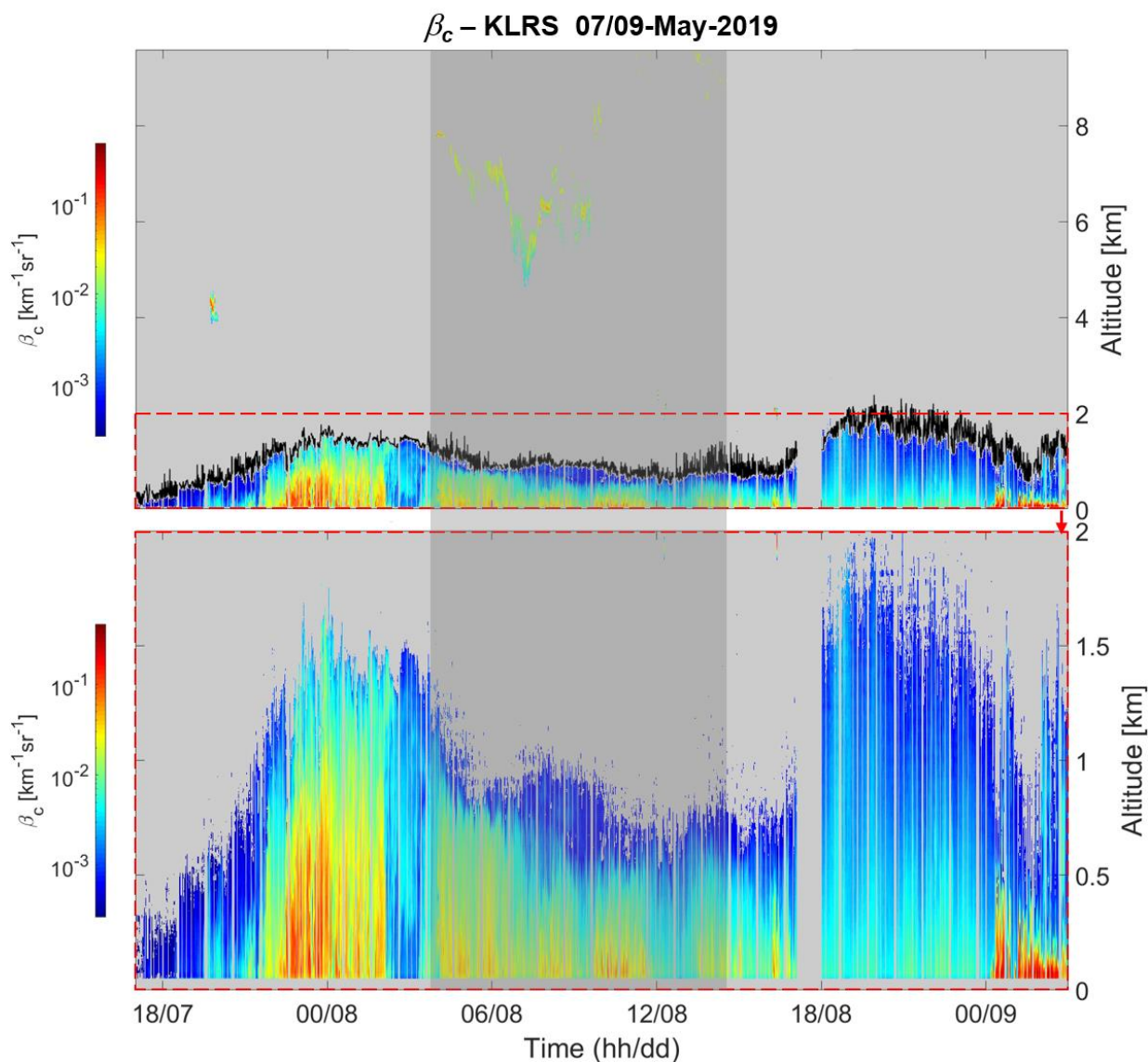
Figure 3: $\beta_c(z)$ profile, from 0.05 to 9.6 km (top panel) and a zoom from 0.05 to 2 km (bottom panel) during a selected time period in May 2019 (the red-dashed rectangles underscore the 0.05 to 2 km range in both panels). The times are UT (local "Pacific daylight" time is 7 hours behind the UT time). The grey background corresponds to lidar profile pixels that are set to NaN (not a number): these are the result of

signal-to-noise ratio (SNR) threshold flags employed to eliminate excessively noisy data (Newsom & Krishnamurthy, 2020). The monotonic black color that is evident at the top of the plume in the upper panel shows the automated estimate of dust layer height (DLH).

## 4.2 Classification of dust events

### 4.2.1 Results of the correlation analysis

In order to investigate the influences on $R_{log}\left(\tau_{dust}^{\ell} \, vs \, v_{dust}(0)\right)$ variability (and thus better understand its impact on the classification methodology) we computed (as discussed in Sect. 3.4) both linear and log space (arithmetic and geometric) correlations as well as the dependence of those correlations on time bin resolution. Sample arithmetic and geometric correlation coefficient values as a function of temporal bin resolution are shown in Supplementary material (S3). Geometric correlation coefficients ($R_{log}$) were typically of the same order as or better than arithmetic coefficients ($R$) in the presence of more than one decade of $\tau_{dust}^{\ell} \, vs \, v_{dust}(0)$ variation : we accordingly used this as support for reporting correlation coefficients in geometric statistics space. This choice was supported by analyzes showing that ground- and satellite-based AOD frequency distributions were better described by geometric means and standard deviations (O'Neill et al., 2000 and Sayer & Knobelspiesse, 2019 and references cited therein).

Aside from the obvious limitations of low-N (low sample number) statistics, no strong dependence on time-bin resolution was found. We accordingly chose to employ the highest bin resolution variant of $R_{log}$ (where the lidar and KLRS OPS measurements are resampled to CIMEL averaging bins of 1 minute and inter sample gaps of 3 minutes) as the basis for our classification analysis (the selection of the high bin-resolution case being also justified on the general principle of wishing to minimize the elimination of high frequency lidar data that might have physical significance).

### 4.2.2 Subclass statistics

The POI subclass results for the complete month of May 2019 are shown in Fig. 4 (b1 and b2) while the corresponding $R_{log}\left(\tau_{dust}^{\ell} \, vs \, v_{dust}(0)\right)$ and $R_{log}\left(\tau_c \, vs \, \tau_{(D \, or \, U)}^{\ell}\right)$ values are shown in Fig. 4 (a1 and a2). As one might expect, the results often show a degree of correlation between the class-determining correlation coefficients (i.e. a degree of covariation between $R_{log}\left(\tau_{dust}^{\ell} \, vs \, v_{dust}(0)\right)$ and $R_{log}\left(\tau_c \, vs \, \tau_{(D \, or \, U)}^{\ell}\right)$). At the same time, there are, for example, two $D_{NRS}$ events of negative $R_{log}\left(\tau_c \, vs \, \tau_D^{\ell}\right)$ (see Sect. 4.2.3 for optical details on one of those events). Details of a May 8 $U_{RS}$ event are discussed in Sect. 4.2.4. We also note the existence of five $D_{GEN}$ events (identified using the lidar profiles of the Supplementary material (S6) as well as the PlanetScope image on May 27).
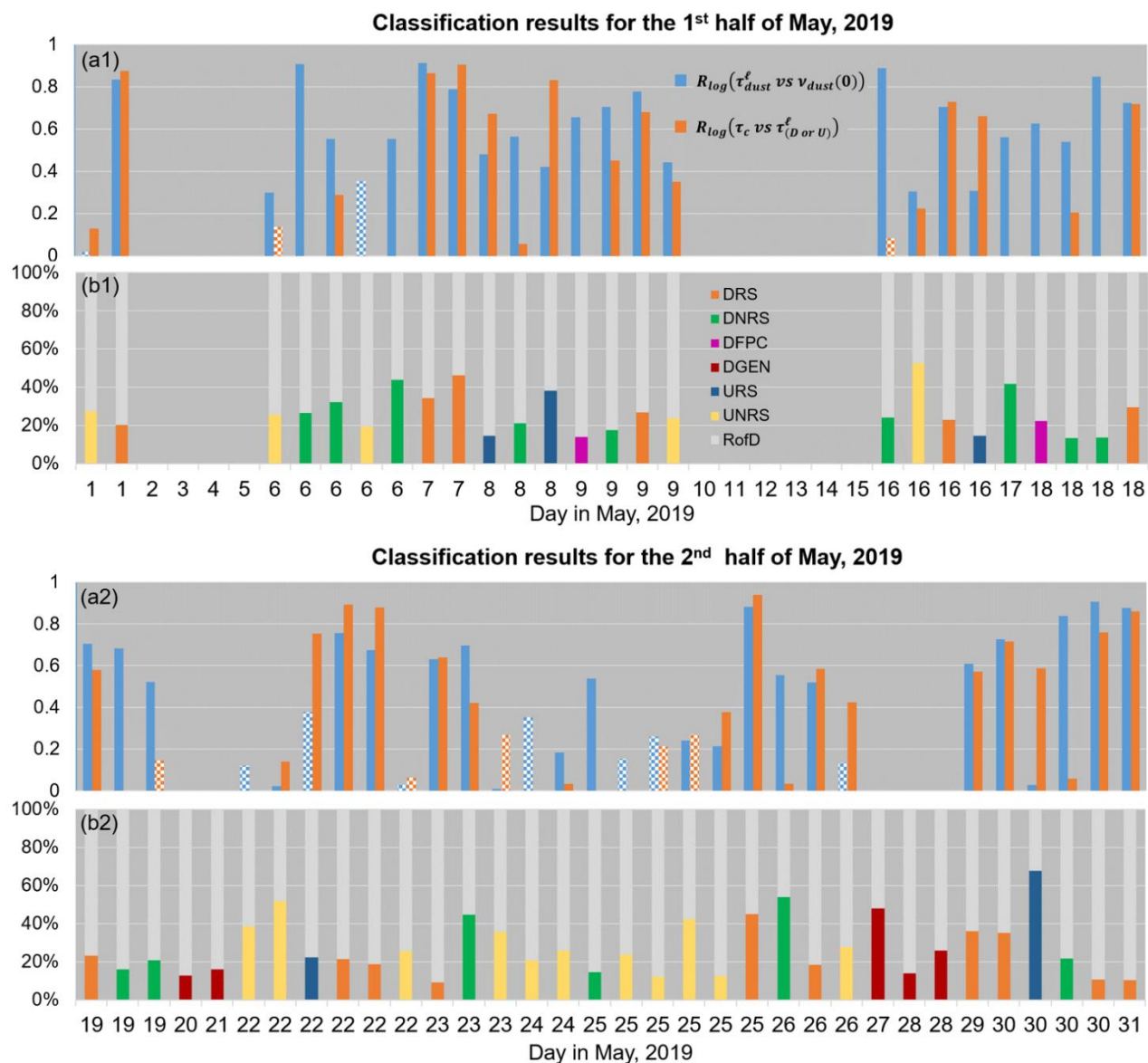
Figure 4: May 2019 results: $R_{log}\left(\tau_{dust}^{\ell} \; vs \; v_{dust}(0)\right)$ and $R_{log}\left(\tau_c \; vs \; \tau_{(D \; or \; U)}^{\ell}\right)$ for the upper profiles (a1 and a2). $D_{RS}$, $D_{NRS}$, $D_{FPC}$, $D_{GEN}$, $U_{RS}$, and $U_{NRS}$ subclasses for the lower profiles (b1 and b2). The subclasses are represented as duty cycles (event duration as a percent of 24 h). The hatched $R$ bars of the a1 and a2 profiles represent negative values. The details on the $R_{log}$ correlation coefficients as well as the $D$ and $U$ subclasses are defined in Sect. 3.5. An overview flow-chart showing the major components of the classification scheme is presented in Fig. 2.

### 4.2.3 Cloud and pseudo-cloud illustrations during class D events

In many cases the CIMEL processing resulted in no or very few AODs during periods when clouds were identified in the lidar profile (this, in spite of there being no nominal cloud screening for the Level 1.0 SDA⁺ product). However, there is a

"triplet" filter at the beginning of the data processing chain which eliminates highly variable triplet ODs during the CIMEL 1 minute bin-averaging period (see Giles et al., 2019). These highly variable ODs are not only restricted to clouds: they also included extremely variable CM dust AODs during periods of the day that were largely cloud-free (what would amount to strong spatially variant dust plumes crossing the FOV of the CIMEL)[10]. This problem was also reported by Evan et al. (2021).

Figure 5 illustrates two types of $D$ subclasses (between the black- and red-dashed vertical lines). The lidar captures cloud and dust intrusions between the black vertical lines (cloud layer ~ 2 km and dust layers below 2 km) during which there are no SDA+ retrievals. This is an example of largely legitimate cloud screening by triplet filtering of AODs prior to promotion to Level 1.0 AODs (the significant high frequency variation of the green $\tau_{cloud}^{\ell}$ curve supports this affirmation). The triplet filtering between the red vertical lines (encompassing a large cloud-free event) retains, on the other hand, a significant number of dust-correlated $\tau_c$ values to yield a $D_{RS}$ event. Note, however, that the Level 1.5 product (not shown) eliminates nearly all retrievals associated with the Level 1.0 $D_{RS}$ event: this amounts to an example of a $D_{FPC}$ event for Level 1.5 AODs (Fig. 4 of Evan et al. (2021) illustrates what is likely a $D_{FPC}$ event resulting from aggressive cloud screening being applied to Level 1.0 AODs). This discrepancy between the Level 1.0 and Level 1.5 subclasses indicates an excessive sensitivity of Level 1.5 cloud screenings to optical variations that are most likely local dust variations. This is, in fact, a situation where it is better to minimize cloud-screening protocols if the ultimate goal is detection and characterization of highly variable local dust.

Another cloud impact example is associated with the two negative $R_{log}(\tau_c \ vs \ \tau_D^{\ell})$ cases referred to above: it is instructive to understand the optical dynamics of one of these cases (both of which were plagued by the presence of multi-altitude cloud). The POI 16-1 event at the beginning of May 16 (cf. the upper profile on page 8 of the Supplementary material, S6) showed strong $\tau_{cloud}^{\ell}$ variation associated with[11] vertically thin but optically thick clouds at <~ 2 km altitude whose triplet impact appeared to create large gaps in the temporal variation of $\tau_c$. In contrast, more homogeneous clouds at ~ 4 km (whose $\tau_{cloud}^{\ell}$ values appear between gaps of the 2 km clouds but which themselves were interspersed with gaps induced by the strong attenuation of the 2 km clouds) sometimes evaded the triplet filtering. The coupling of these two different types of cloud interference did much to eliminate any possible covariation between the remaining $\tau_c$ points and $\tau_D^{\ell}$.

---

[10] At the other cloud screening extreme are false negative clouds associated with homogeneous clouds such as cirrus that go undetected. V3 processing incorporated some significant changes in an attempt to deal with this problem (Giles et al., 2019).

[11] ~ 100 m in vertical thickness and optical depths >~ 1. The $\beta_{cloud}$ values associated with those clouds are removed in the lower profile of slide 8 (as part of the DLH process).
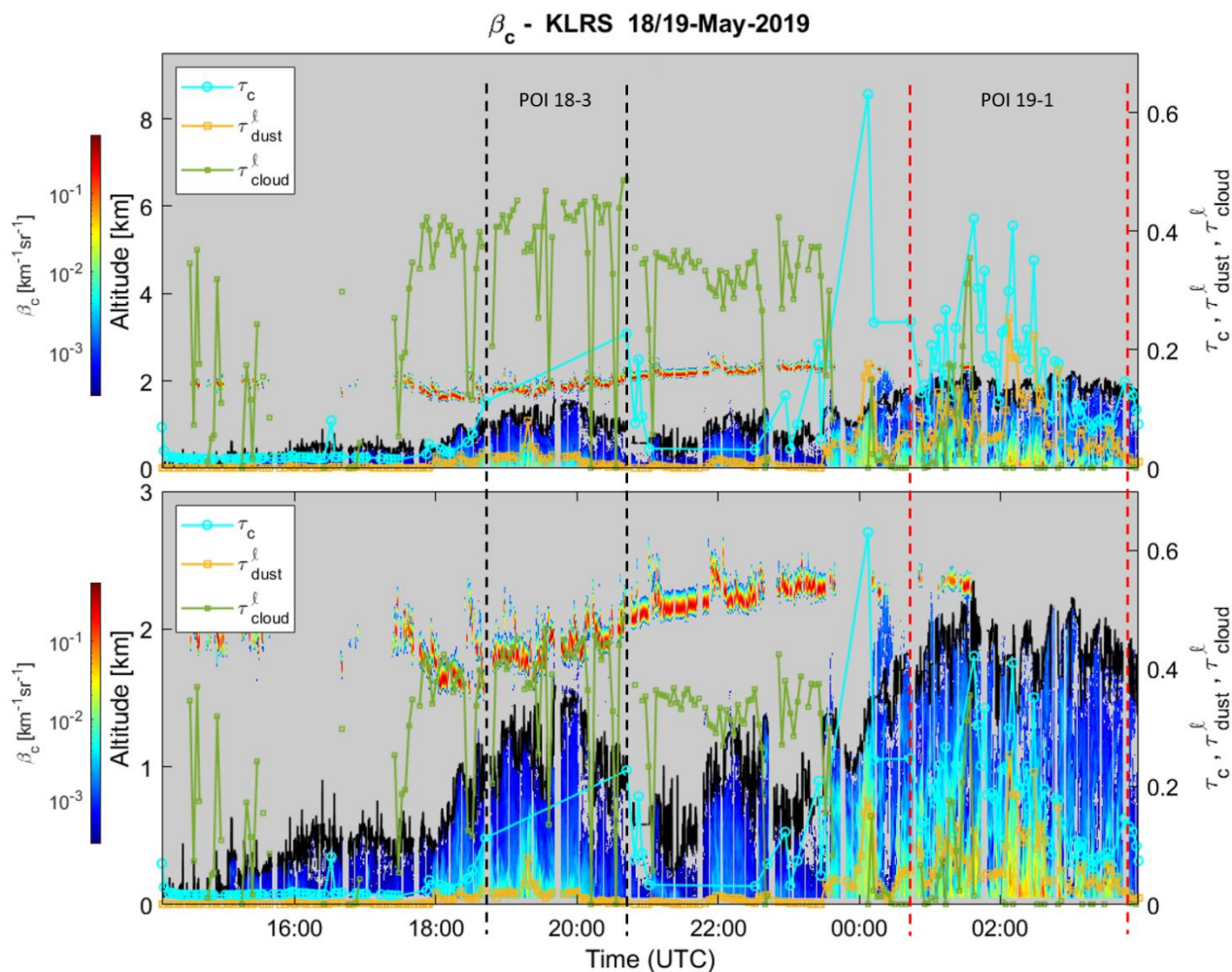
Figure 5: **D** subclass events of May 18, and the beginning of May 19, 2019. The top profile above shows the entire lidar altitude range while the bottom profile is restricted to the 0–3 km range in order to better appreciate the details of the dust plume (below ~ 2 km) and the thin cloud layer hovering around 2 km. The black and red-dashed vertical lines encompass two **D** subclass events (POI 18-3 and POI 19-1). The former event shows that no $\tau_c$ value survived the triplet filtering while the latter $\boldsymbol{D_{RS}}$ case indicates substantial $\boldsymbol{\tau_c}$ $\boldsymbol{vs}$ $\boldsymbol{\tau_D^\ell}$ correlation $(\boldsymbol{R_{log}(\tau_c\ vs\ \tau_D^\ell)} = 0.58)$.

### 4.2.4 Remote sensing threshold for the detection of local dust

Figure 6 shows a plot of $\tau_{dust}^\ell$ vs $v_{dust}(0)$ for all class $D$ and $U$ events during May of 2019. The graph suggests, for a certain fraction of the events, a $\tau_{dust}^\ell$ insensitivity to $v_{dust}(0)$ values below an apparent "bottoming out" threshold (upper limit) ~$10^{-11}$ µm³µm⁻³. However the subclass scattergrams of the Supplementary material (S4) suggest a more nuanced upper limit threshold: the $U_{RS}$ and $U_{NRS}$ scattergrams, in particular, show upper-limit $v_{dust}(0)$ thresholds that can be anywhere in the $10^{-11}$–$10^{-10}$ µm³µm⁻³ range with a respective $\tau_U^\ell$ range of 0.001–0.1. AboEl-Fetouh et al. (2020) showed pan-Arctic $\tau_c$ values (regional-scale, multi-year geometric means) that appeared to be robustly sensitive to natural events whose $\tau_c$ variation was as

360   small as ~ 0.001. That the $\tau_U^\ell$ bottoming out values of the $U_{RS}$ and $U_{NRS}$ scattergrams are generally well above this value suggests that the apparent lack of $\tau_U^\ell$ variability is attributable to very local, near-surface dust dynamics that are at the margins of column-scale detectability. This suggestion is consistent with the observation of Huck et al. (2023) on the importance of local scale variability during Lhù'ààn Mân' dust storms.

The POI 8-3 event of Fig. S1 underscores the relevance of the $U_{RS}$ subclass assignment (of $R_{log}(\tau_c \ vs \ \tau_U^\ell)$ being large):

365   the apparent $\tau_U^\ell$ bottoming out of all the point clusters in the $U_{RS}$ scattergram of Fig. S4 is more about an apparently narrow spread driven by the densely packed $\tau_U^\ell$ log scale. The appearance of the POI 8-3 lidar profile and the temporal covariation of $\tau_c$ and $\tau_U^\ell$ (associated with the orange points of Fig. S4) is strongly suggestive of an optically weak dust plume for which the covariation of $\tau_c$ and $\tau_U^\ell$ is not some statistical artefact. This does not detract from the argument of local scale $v_{dust}(0)$ variability being uncoupled from the columnar variability: it simply says that the physical significance of the

370   columnar variability can occur within the (apparently narrow) $\tau_U^\ell$ spread of the point clusters in the $U_{RS}$ scattergram.
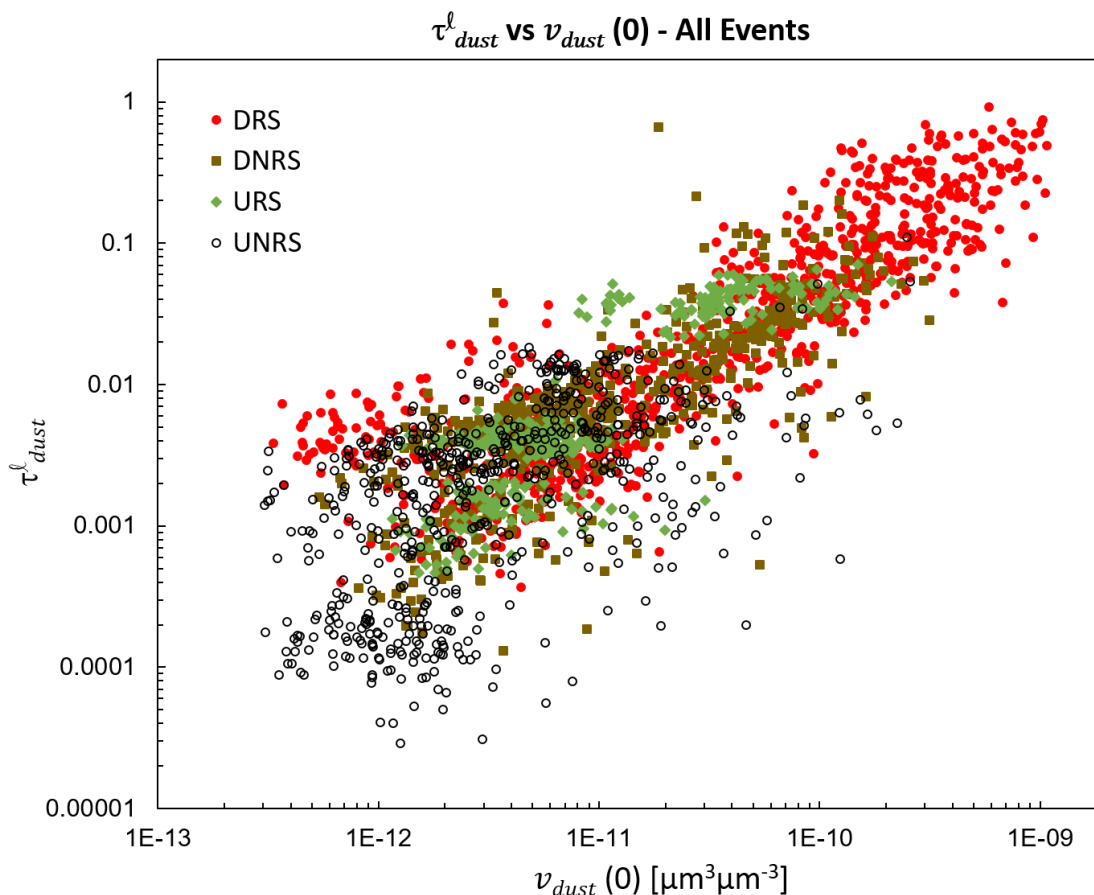
Figure 6: Plot of $\boldsymbol{\tau_{dust}^\ell}$ vs $\boldsymbol{v_{dust}(0)}$ for all class $\boldsymbol{D}$ and $\boldsymbol{U}$ events during May of 2019. Note that this ensemble of data excludes points belonging to the special $\boldsymbol{D_{FPC}}$ and $\boldsymbol{D_{GEN}}$ subclasses.

### 4.3 Parameterization of dust plume properties

375   **4.3.1 Lidar ratio**

#### 4.3.1.1 Prescribed lidar ratio

The CM $r_{eff}$ ($r_{eff,c}$) values for the whole month of May 2019 were calculated for all individual KLRS OPS PSDs that were part of class $D$ POI events. A temporal plot of those individual $r_{eff,c}$ ($r_{eff,D}$) values can be seen in Fig. 7. The averaged class $D$ results for the month of May were (as per the Fig. 7 legend) found to be: $\langle r_{eff,D} \rangle \pm \sigma_D(r_{eff,D}) = 2.26 \pm 0.23 \ \mu m$.
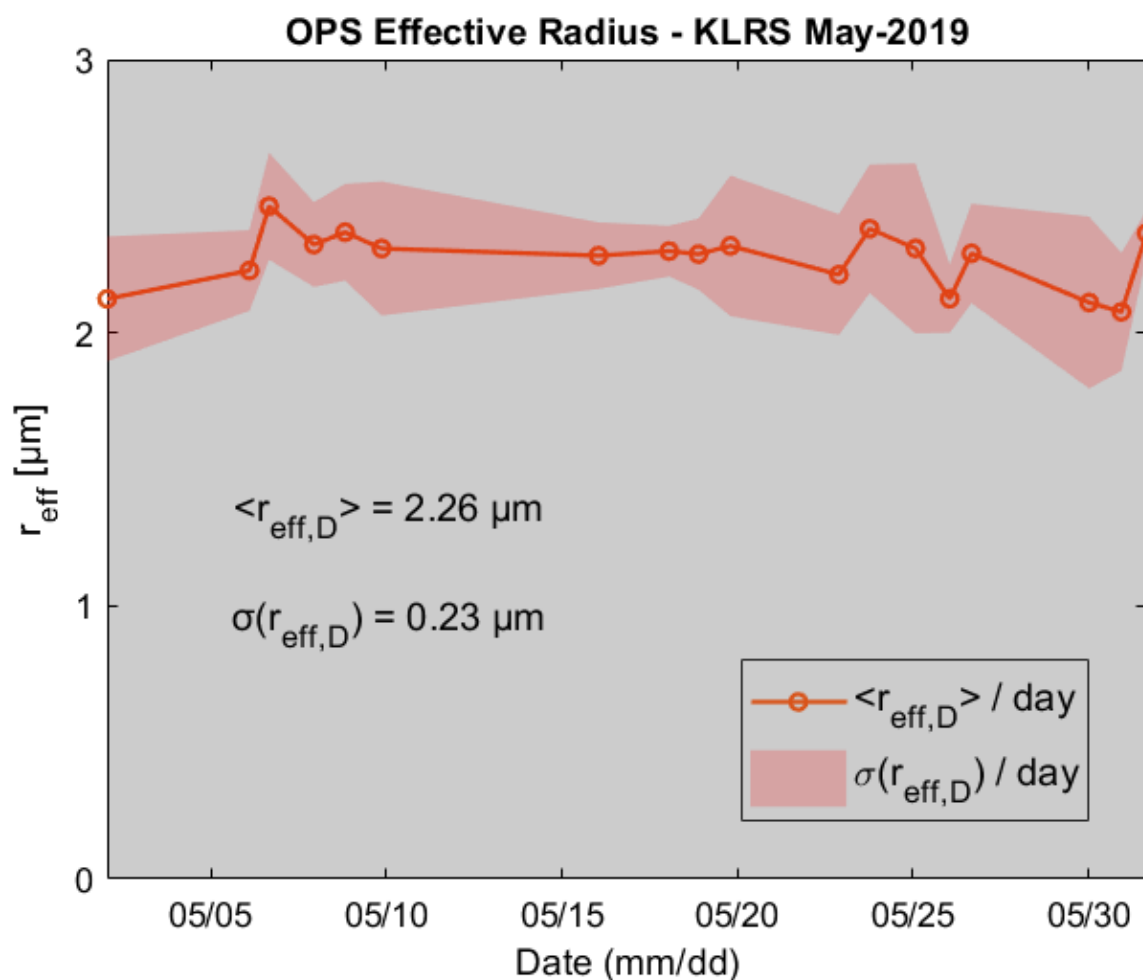
Figure 7: Variation of OPS-derived, class-$\boldsymbol{D}$, $\boldsymbol{r_{eff}}$ values during the month of May 2019.

Clay, feldspar, and then quartz minerals are the major constituents of the PM10 dust particles from the emissions in the Kluane Lake region (Bachelder et al, 2020; King, 2023). To derive the mean refractive index and the uncertainty for those values, we followed the method of Baldo et al. (2020) using the volumetric-average refractive index based on the relative

385  volume fraction weighted refractive indices of the minerals found within the dust sampled at the site, through X-ray diffraction, assuming an internally mixed sample (Formenti et al., 2014). The result, which we took to be representative of the Lhù'ààn Mân'region, was a mean refractive index of $n = n_0(\pm\Delta n_0) - k_0(\pm\Delta k_0)\,i = 1.5371(\pm 0.0028) - 0.00075(\pm 0.00072)\,i$ at the 1.548 µm lidar wavelength.

Figure 8 shows the range of lidar ratio curves given the mean and uncertainties of the down valley estimates of refractive

390  index and a 0–12 µm range of $r_{eff,D}$ values (the OPS-derived $r_{eff,D}$ values and their uncertainties appear as orange circles). All lidar ratios were computed using a (spherical particle) Mie code (Evans, 1994) integrated over a lognormal PSD (see Sokolik & Toon, 1999 for a typical formulation and values of that analytical PSD). We employed Sokolik & Toon's geometric standard deviation for dust ($"\sigma_j"  = 2$) and forced the lognormal geometric mean ("$r_{0j}$") to yield a computed lognormal-PSD effective radius that matched the OPS-derived $\langle r_{eff,D}\rangle$ values. The colored curves of Fig. 8 nicely demonstrate the impact of

395  the real and imaginary parts of the refractive index on the lidar ratio computations (somewhat balanced impact at small $r_{eff,D}$ in the neighbourhood of the OPS derived values of $r_{eff,D}$ with a much stronger impact of the complex part of the refractive index at larger radii). This yielded a prescribed lidar ratio estimate of $S_D^p = 10.7 \pm 0.9$ sr (where the uncertainties were derived by combining the $r_{eff,D}$ and refractive index uncertainties).
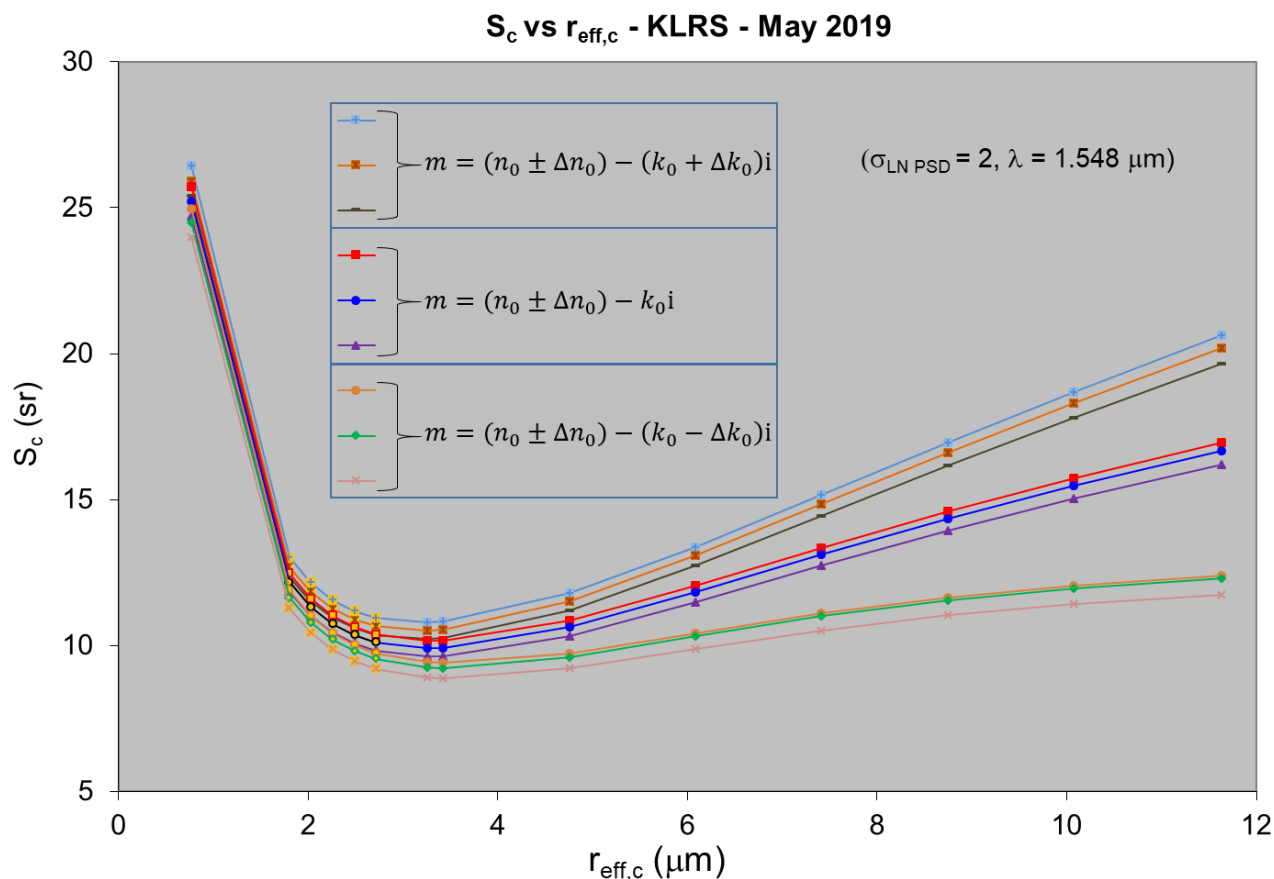
Figure 8: Mie (spherical-particle) computations of lidar ratio based on the refractive index ($n$) value from above. The orange circles represent $r_{eff,D}$ changes from $\langle r_{eff,D} \rangle - 2\sigma(r_{eff,D})$ to $\langle r_{eff,D} \rangle + 2\sigma(r_{eff,D})$ in increments of $\sigma(r_{eff,D})$. The refractive index parameters of the figure are $n_0 = 1.5371, \Delta n_0 = 0.0028, k_0 = 0.00075,$ and $\Delta k_0 = 0.00072$. $\sigma_{LN\ PSD}$ refers the standard deviation of the lognormal PSD that was employed in the Mie computations. A "c" subscript is employed (rather than "$D_{RS}$") because of the limitations of the graphing program.

**4.3.1.2 Evaluation / validation of the prescribed lidar ratio**

Individual ($\log \tau_{D_{RS}}$ $vs$ $\log \tau_{D_{RS}}^{\ell}$) derived $S_{D_{RS}}$ values for each $D_{RS}$ event were computed as per Appendix A1 (i.e., weighted best estimates of separate $S_{D_{RS}}$ computations for each event where weights are defined by the inverse square of $S_{D_{RS}}$ regression residuals). The overall weighted result for the entire month of May 2019 was $\langle S_{D_{RS}} \rangle_\omega \pm \sigma_w(S_{D_{RS}}) = 28.0 \pm 3.3$ sr. The weighted mean, $\langle S_{D_{RS}} \rangle_\omega$, is roughly three times the $S_D^p$ value of $10.7 \pm 0.9$ sr reported above. While the overall apparent effect of the weighting scheme, as seen in Fig. S5, was to greatly reduce the variation as a function of increasing weight it did not objectively achieve satisfactory agreement with $S_D^p$. A measure of closer agreement with the $S_D^p$ value was

obtained by setting a higher standard on the $\log \tau_c^\ell$ vs $\log \tau_c$ regressions or the amplitude of the slant path lidar optical depth[12]: $\langle S_{D_{RS}} \rangle_\omega$ values of $19.1 \pm 2.3$ sr and $20.3 \pm 2.6$ sr for $R_{log} > 0.9$ or slant path optical depth $> 0.05$ respectively. The positive bias is eliminated (at the margins of significance) if we subjectively select a single, maximally-significant POI[13] for

415  which $\langle S_{D_{RS}} \rangle_\omega$ was $15.4 \pm 4.7$ sr ($15.4 - 4.7 = 10.7$ sr). We note that the comment by Huck et al. (2023) concerning the frequent missing of plumes by the CIMEL (or presumably only capturing a portion of the plume in the CIMEL FOV) is actually a counter dynamic to the positive bias: a problem of partially missing the plume would actually help to reduce the bias.

Given the persistence of this positive bias we sought to determine whether $S_D^p$ could, in fact, be underestimated. A significant increase in its computed value can be obtained by assuming the general presence of larger, optically-significant

420  dust particles in the plumes. Figure 8 indicates that an $r_{eff,D}$ value ~ 11–12 μm and the higher value of the imaginary index of refraction determined from the dust speciation result would push the $S_D^p$ to values ~ 20 sr (a value commensurate with the "higher standard" argument in the previous paragraph). The OPS instrument with its upper limit of 5 μm radius (see Sect. 4.3.2.1 below) is incapable of measuring such a PSD contribution while the few AERONET inversions that were available showed a dust mode of increasing radius (up to 7 μm) with increasing (but weak) values of dust optical depth (see the following

425  section). Ranjbar et al. (2021) reported the presence of dust particles >~ 15 μm radius[14] for CloudSat / CALIOP (DARDAR) retrievals over Lake Hazen dust plumes in the Canadian high Arctic (a drainage-basin environment similar to that of Lhù'ààn Mân'). At southern latitudes, optically-significant lidar profiles whose volume-median radius was >~ 8 μm have been observed for near-source Saharan dust plumes (the Fig. 13, May 20–28 results of Weinzierl et al., 2009 and, as evidence of optical significance, the corresponding column averaged lidar ratios of Esselborn et al., 2009).

430  **4.3.2 AERONET inversions**

Table 1 lists key AERONET CM inversion products acquired during D class events for the month of May 2019 (optically based inversion products that were spectrally extrapolated to the 1.548 μm lidar wavelength from values at the shorter inversion wavelengths). The relatively few retrievals underscore the sometimes-frustrating disparity of dealing with the information rich AERONET-inversion product when it is associated with few inversions during an event of interest (coupled with the fact that

435  the CM AOD were generally weak: $\tau_{c,inv} < 0.15$). This speaks to the difficulty in extracting significant numbers of AERONET retrievals even on the Table 1 days with the largest $\tau_{c,inv}$ values. However, if the information we want is of an intensive-parameter nature (effective radius, PSD radius attributes like PSD-peak positions, etc.) then we can aspire to extract representative values that vary little across a month (that don't need to be monitored at a high sampling rate).

---

[12] $\langle m \rangle \langle \tau_c^\ell \rangle$ where $\langle m \rangle$ is the POI-averaged airmass of the sun: the hypothetical case where the lidar is looking through a plane parallel plume at the same zenith angle as the sun.

[13] May 25 (POI 25-6) with an $R_{log}$ value of 0.946

[14] the lower limit of 15 μm being determined by CloudSat radar detection limitations

Table 1: AERONET May 2019 CM inversion products for all retrievals classified as $D_{RS}$ events (ordered according to decreasing $\tau_{c,inv}$).
440 With respect to the single $U_{RS}$ (POI 8-3) case: the rather dominant $\tau_{c,inv}$ value and the appearance of its lidar profile in the Supplementary material (S6) suggest that it is most likely a dust event (it could, for example, be attributed a $D_{GEN}$ subclassification). The $\tau_{c,inv}$ product was derived from a spectral extrapolation (using log-log regressions) from the four AERONET inversion wavelengths to the 1.548 µm lidar wavelength. The colors associated with the different dates represent retrievals for the 6 largest $\tau_{c,inv}$ values (the same colors are used to identify the associated PSDs of Fig. 9).

| Date (2019) | Time (UTC) | POI | $\tau_{c,inv}$ | Sub-class | $V_{c,inv}$ ($\mu m^3 \mu m^{-2}$) | $r_{eff,c,inv}$ (µm) | $m_r$ | $m_i$ |
|---|---|---|---|---|---|---|---|---|
| 08-May | 20:12:51 | 8-3 | 0.144 | $U_{RS}$ | 0.778 | 3.262 | 1.600 | 0.001 |
| 02-May | 00:48:49 | 1-2 | 0.048 | $D_{RS}$ | 0.130 | 1.816 | 1.597 | 0.007 |
| 02-May | 00:12:48 | 1-2 | 0.041 | $D_{RS}$ | 0.096 | 1.639 | 1.600 | 0.005 |
| 07-May | 19:12:50 | 7-1 | 0.028 | $D_{RS}$ | 0.053 | 1.317 | 1.619 | 0.003 |
| 09-May | 22:12:50 | 9-3 | 0.023 | $D_{RS}$ | 0.069 | 1.880 | 1.600 | 0.004 |
| 07-May | 18:12:51 | 7-1 | 0.020 | $D_{RS}$ | 0.038 | 1.318 | 1.600 | 0.001 |
| 22-May | 17:48:51 | 22-4 | 0.016 | $D_{RS}$ | 0.050 | 1.854 | 1.525 | 0.008 |
| 22-May | 19:12:52 | 22-4 | 0.016 | $D_{RS}$ | 0.044 | 1.692 | 1.546 | 0.010 |
| 22-May | 18:12:53 | 22-4 | 0.015 | $D_{RS}$ | 0.045 | 1.741 | 1.504 | 0.008 |
| 25-May | 22:12:50 | 25-6 | 0.015 | $D_{RS}$ | 0.037 | 1.656 | 1.600 | 0.011 |

445

### 4.3.2.1 Intensive parameters from AERONET inversions

Figure 9 shows the set of PSDs corresponding to the retrievals of Table 1. One can observe bimodal CM peak positions near 1.3 and 5.0 / 6.6 µm (bin centers of respectively bins 13 and 18 / 19 of the AERONET inversion). In general, there appears to be a trade-off between the 1.3 and 5.0 / 6.6 µm peaks depending on the strength of the relative contributions to each peak.

450 AboEl-Fetouh et al. (2020) ascribed the presence of a 1.3 µm component to the springtime incursion of Asian dust over six AERONET stations spread across the North American and European Arctic (springtime being largely represented by April and May in their monthly averaged PSDs). The 6 largest $\tau_{c,inv}$ cases of Table 1 arguably represent the strongest local dust contributions. Four of these values are more dominated by the 5.0–6.6 µm peak while the other two are sufficiently weak to be dominated by a stronger 1.3 µm peak. The $r_{eff,c}$ values of Table 1 represent a compromise driven by the 1.3 and 5.0–6.6

455 µm peak positions (where the importance of the latter peak tends to increase with increasing $\tau_{c,inv}$). These $r_{eff,c}$ values (with an average of 1.87 µm) are somewhat less than the OPS-derived mean of 2.26 µm.

The suggestion that the AERONET 1.3 µm PSD peak is due to Asian dust needs to be contextualized by a relatively consistent, neighbouring peak at the 1.75 µm OPC bin (radius) center that was often recorded by the two DV units (see the Supplementary material (S7) to observe the daily ensemble of OPS PSDs at KLRS and the OPC PSDs at the DV site on the

460 six days corresponding to the 6 largest $\tau_{c,inv}$ events of Table 1). That peak was not observed by the OPS: the KLRS ensemble

of PSDs on the six days in question could be best described as a broad modal feature whose form was quite stable but whose amplitude was highly variable. The broad nature of that modal feature inhibits any simple characterization (one cannot readily select a significantly robust modal peak that stands above the other PSD values in neighbouring bins). In fact, it appears to be common to the KLRS and DV sites if one views the 1.75 µm DV peak as a perturbation atop of that feature. Given the lack of

465 even a 1.75 µm peak at the KLRS site and the ubiquitous nature of the 1.3 µm peak over the North American and European Arctic (AboEl-Fetouh et al., 2020) it is likely that the 1.3 µm AERONET peak is associated with springtime Asian dust. Finally, we would note that the broad CM feature might well be dynamically associated with the 5.0–6.6 µm AERONET inversion peak (with the OPS effective radius arguably being smaller than the AERONET inversion effective radius due to its 4.5 µm, bin-center, cutoff radius).

470 The significance of this result (in spite of our intensive parameter arguments at the beginning of this section) is necessarily brought into question by only having a handful of PSD retrievals over the whole month of May (and only one single retrieval with a dominant 6.6 µm component). In addition to this constraint on the number of retrieved PSDs, the $\tau_{c,inv}$ contribution of a 6.6 µm peak will generally be dominated by the $\tau_{c,inv}$ contribution of the 1.3 µm peak[15]. The few retrievals and their low $\tau_{c,inv}$ values are likely attributable to the cloud screening process of the AERONET inversions (whose constraints are

475 commonly known to be more stringent than the cloud-screening protocol for AODs; this arguably amounts to the assignment of a $D_{FPC}$ subclass in the case of the inversion processing stream).

The values of the real part of the refractive index in Table 1 are clearly susceptible to retrieval saturation issues (most notably the evident flatlining at a value of 1.6). The values of the imaginary part of the refractive index are highly variable (standard deviation at 1020 nm that is ~10 times the abovementioned, clay-mineral value of Sokolik & Toon, 1999). In general,

480 one cannot ascribe much confidence to the May 2019 refractive index values: the AERONET U27 inversion-error product described by Sinyuk et al. (2020) shows no values (corresponding to a code of "-999") for the real and imaginary parts of the refractive index (and the derived single scattering albedo). The authors indicate that no U27 values are reported "for any of the retrieved parameters" subject to a "boundary hit" (lower and upper limits of 1.33 to 1.6 represent such boundaries for the real part of the refractive index). Finally, we would note that, the comments made above concerning the behavior of the Fig. 9

485 PSDs are virtually unchanged if we restrict the retrieved PSDs to those that are not subject to "boundary hits" of the real part of the refractive index.

---

[15] It is easy to approximately show, using Mie calculations and a refractive index ~ 1.6 (employing the approximate AERONET retrieval value for optical consistency) that the per-particle extinction efficiency associated with the AERONET particle-volume distribution (whose product, integrated over radius, would yield $\tau_{c,inv}$) is significantly larger at 1.3 µm radius.

![Figure 9: PSD Level 1.5 May-2019. A plot of dv(r)/dln(r) [µm³ µm⁻²] versus Radius (r) [µm] showing multiple PSD curves.]

**PSD Level 1.5   May-2019**
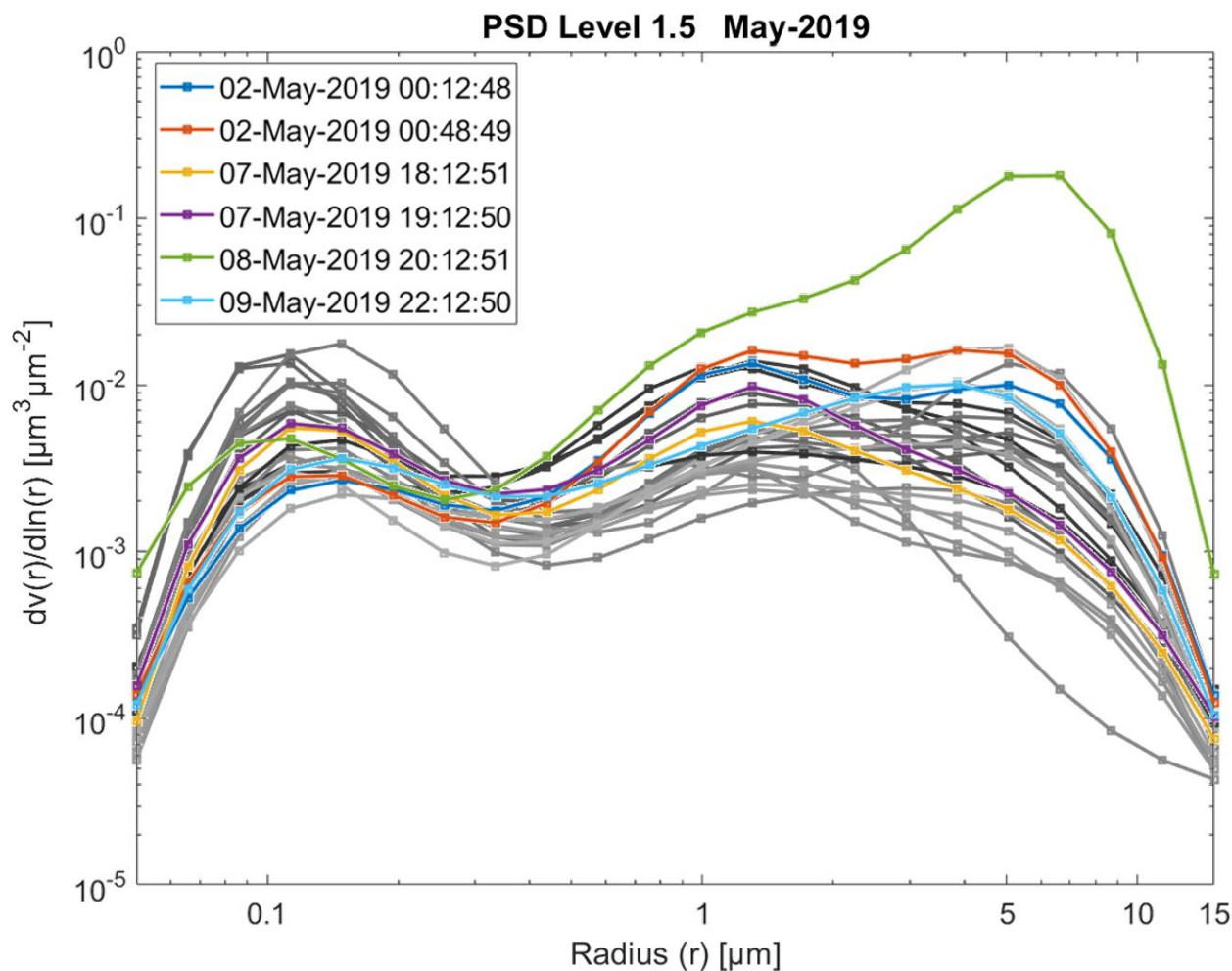
Legend:
- 02-May-2019 00:12:48
- 02-May-2019 00:48:49
- 07-May-2019 18:12:51
- 07-May-2019 19:12:50
- 08-May-2019 20:12:51
- 09-May-2019 22:12:50

Figure 9: AERONET-inversion PSDs ($dV/dlnr$) corresponding to the retrievals listed in Table 1 (the colored PSD curves correspond to the colors of Table 1). The grey-colored curves include the non-colored entries of Table 1 as well as all other May 2019 retrievals that were not assigned to the $D_{RS}$ subclass.

### 4.3.3 The remote sensing detectability of fine mode dust

The FM part of the KLRS and DV PSDs clearly covary with their CM analogue (see the PSDs in the Supplementary material, S7). This suggests a weak but robust presence of FM dust. While FM dust is likely a relatively minor optical component (especially at the lidar wavelength), its transport dynamics would likely differ from CM dust, and it could add to the long-distance spread of local dust in the Arctic. Figure 10 is a temporal plot of the 500 nm $\tau_f$ and $\tau_c$ AERONET product, as well the FM-integrated OPS particle-volume concentration ($\nu_f(0)$) on the $D_{RS}$ (POI 7-1 and POI 7-2) day of May 7, 2019[16].

---

[16] The limitation of $\tau_c$ to 500 nm applies only to this specific case: otherwise $\tau_c$ is computed at the lidar wavelength of 1.548 µm in the rest of the paper

Significant correlation of low and high frequency can be observed between $\tau_f$ and $\tau_c$ and between $\tau_f$ and $\nu_f(0)$). It should be noted that one expects a significant $\tau_f$ background (bottoming out) in the Arctic (see AboEl-Fetouh et al., 2020 for example) and this would tend to disrupt the dust-based correlation with $\tau_c$ and with $\nu_f(0)$ prior to the beginning of the dust event (around

500    19:20 UT). This suggests that a satellite-based, AOD remote sensing technique at a few visible and near IR wavelengths (the equivalent of what is employed by AERONET to extract $\tau_f$ and $\tau_c$ at 500 nm) would have a reasonable chance of extracting a $\tau_f$ dust component and thus contribute to the type of spatial information that one could aspire to extract from satellite-based remote sensing (one can, specifically aspire to extract the MODIS fine mode fraction product of $\tau_f/(\tau_f + \tau_c)$ that can then be converted to a $\tau_f$ estimate)
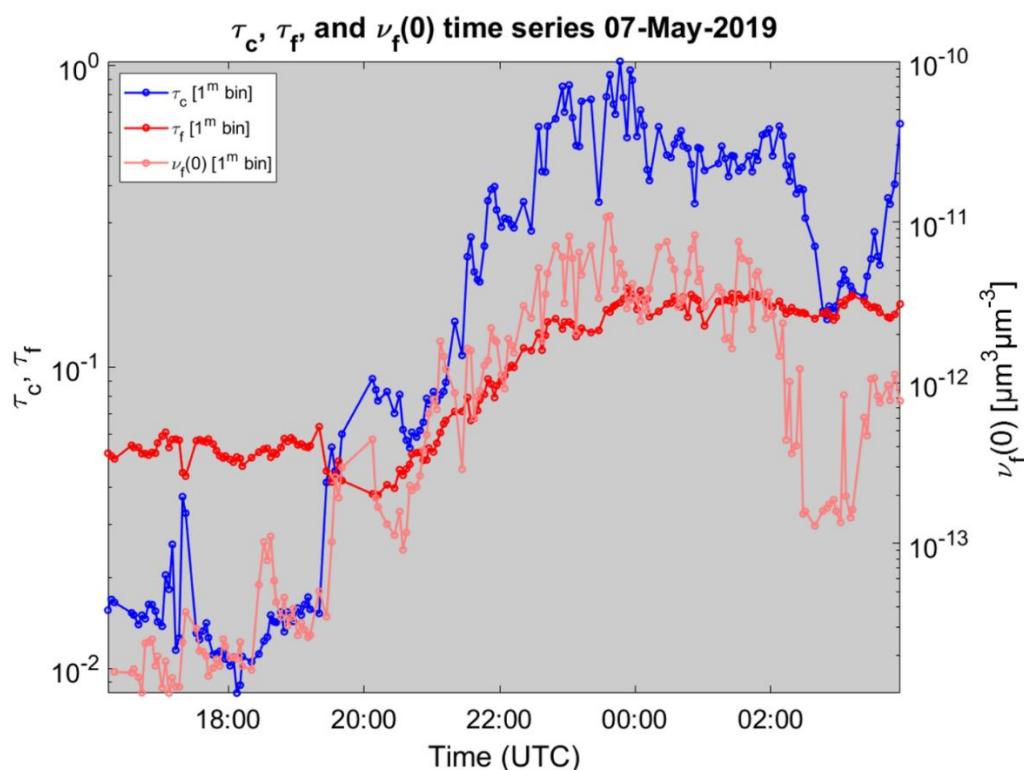
505

Figure 10: Temporal plot of $\tau_f$ and $\tau_c$ (500 nm) retrievals along with KLRS OPS surface particle-volume FM concentration $\nu_f(0)$ on May 7, 2019. The $\nu_f(0)$ data has been resampled to the 1 minute ("$1^m$") AERONET bins (with intersample times of 3 minutes).

## 5 Conclusions

We reported on an automated dust classification scheme for which the first steps were the derivation of the dust plume
510    height followed by the definition of a class of optically significant (class "D") dust events. This higher-level classification scheme employed short-wave infrared (1.548 µm) lidar profiles (that were predominantly sensitive to coarse mode (CM)

particles) coupled with surface-based microphysical measurements of CM particle-volume concentration. We defined two class-$D$ subclasses ($D_{RS}$ and $D_{NRS}$) as well as two complementary classes ($D_{GEN}$ and $D_{FPC}$): these represented, respectively, events that could be remotely sensed from a passive ground-based (AERONET-type) spectral AOD sensor (and thus, for

515   example, could likely be remotely sensed by a passive satellite sensor), dust events that could likely not be remotely sensed (NRS), dust events that were identified using data other than OPS data (and/or qualitative evidence such as RGB satellite images) and events that could not be remotely sensed because they were classified as clouds and thus eliminated from analytical consideration by the AERONET cloud screening protocol. We also defined an unclassified ($U$) class: a $U_{RS}$ sub-class represented events whose surface-based CM particle-volume concentration measurements were speculated to be excessively

520   influenced by local dust dynamics (i.e. not in the same dynamics scale as the remotely sensed (columnar) dust optical depths). The associated lack of dust sensitivity was estimated to have an upper limit threshold to be roughly in the $10^{-11}$–$10^{-10}$ µm³µm⁻³ range corresponding respectively to a CM optical depth of 0.001 to 0.1.

The average OPS effective radius of class-$D$ events as measured at the KLRS site (near the CIMEL and lidar instruments) during the month of May 2019 was estimated to be $2.26 \pm 0.23$ µm. A value of dust refractive index at the lidar wavelength

525   was estimated as $1.5371(\pm0.0028) - 0.00075(\pm0.00072) i$ from an analysis Lhù'ààn Mân' dust speciation classes. A prescribed lidar ratio of $10.7 \pm 0.9$ sr was derived from Mie computations employing the OPS-derived effective radius average and the computed refractive index information as input. The CIMEL-derived lidar ratio showed a positive bias that was anywhere from two to three times the prescribed ratio depending on QA constraints placed upon the statistical data employed for its derivation. The persistence of this positive bias led to a hypothesis that the prescribed value could be increased to the

530   CIMEL-derived values of 20 sr by hypothesizing the presence of optically significant dust particles at an effective radius of ~ 11–12 µm. This large-particle hypothesis is not incoherent with OPS measurements (such a particle size is greater than its 4.5 µm upper limit) and is coherent with the fact that the AERONET PSD retrievals showed a CM whose peak radius increased with increasing dust optical depth.

AERONET inversions were few and far between (and generally weak in terms of $\tau_c$ amplitude during the whole month of

535   May 2019). The available inversions showed bimodal CM PSDs with (AERONET bin-center) peaks at radii ~ 1.3 µm and 5.0–6.6 µm and a tendency to be progressively more dominated by the latter peak as $\tau_{c,inv}$ increased. Those larger $\tau_{c,inv}$ values generally occurred during $D_{RS}$ events. The smaller 1.3 µm radius peak was, we argued, likely to be the ubiquitous CM peak that AboEl-Fetouh et al. (2020) ascribed to springtime Asian dust. The latter 5.0–6.6 µm peak is arguably associated with local Lhù'ààn Mân' dust peak represented by a broad 2.0–4.5 µm peak in the KLRS OPS data (but, arguably, of lesser effective

540   radius because of the 4.5 µm (bin-center) cutoff of the OPS PSDs).

Finally, we discussed the possibility of extracting a FM dust component using satellite-based remote sensing. This could yield a unique spatial perspective on the opto-physical dynamics of FM dust: a component that is not well understood (see, for example, Cottle et al., 2013) but that might well play an important role in the spread of dust around the Arctic. Moving beyond

the relatively coarse spatial resolution of the workhorse MODIS sensor, both the CM and FM AOD dust products could be
545   derived for high spatial resolution satellites such as those of the PlanetScope constellation.

**6 Appendices**

**Appendix A1. Theoretical background for $S_c^p$ validation**

Let $S_c^p$ be the current prescribed (constant) value of the dust lidar ratio that was employed to compute $\tau_c^\ell$ ($\tau_c^\ell = S_c^p \, \tau_{\beta_c}$)[17].
The AERONET derived value ($S_c$) for the $D_{RS}$ class would then be:

$$S_c = \frac{\tau_c}{\tau_{\beta_c}} = \frac{\tau_c}{\tau_c^\ell}\frac{\tau_c^\ell}{\tau_{\beta_c}} = \frac{\tau_c}{\tau_c^\ell} S_c^p \tag{A1}$$

If we are employing $\log \tau_c^\ell$ vs $\log \tau_c$ regressions over the POI then[18];

$$\log \tau_{c,reg}^\ell = a \, \log \tau_c + b \text{ where a and b are the regression slope and intercept. Accordingly;} \tag{A2a}$$

$$\frac{\tau_{c,reg}^\ell}{\tau_c} = 10^b \, \tau_c^{a-1} \tag{A2b}$$

Employing equation (A2b) in the "reg" version of equation (A1) yields;

$$S_{c,reg} = \frac{\tau_c}{\tau_{c,reg}^\ell} S_c^p = S_c^p \, 10^{-b} \, \tau_c^{1-a} \tag{A2c}$$

This corresponds to a situation where a given data pair, $\left(\tau_c, \tau_c^\ell\right)$ is forced to lie on the regression line (i.e. equation $(A2a)$
is employed to compute the point $\left(\tau_c, \tau_{c,reg}^\ell\right)$). An objective and pragmatic quality indicator of the lidar ratio would be the
lidar ratio residuals ("subscript "r") given by;

$$\Delta S_{c,r} = S_c - S_{c,reg} = \frac{\tau_c}{\tau_c^\ell} S_c^p - \frac{\tau_c}{\tau_{c,reg}^\ell} S_c^p = \tau_c S_c^p \left(\frac{1}{\tau_c^\ell} - \frac{1}{\tau_{c,reg}^\ell}\right) \tag{A3}$$

560   where $S_c$ is the $S_c$ of Eq. $(A1)$ and where one would compute the average ( $\langle \Delta S_{c,r} \rangle$ ) and standard deviation ( $\sigma\left(\Delta S_{c,r}\right)$ ) over
each POI. In practice, there are large variations in $\Delta S_{c,r}$ and attendant large variations of $S_c$. Weights defined as $\omega =$
$100 \times 1/\left(\Delta S_{c,r}\right)^2$ are an indicator of confidence in a given $S_c$ value which places considerably more confidence on $\left(\tau_c, \tau_c^\ell\right)$
points that are close to the regression line (the weighting factor is inspired by the classical standard deviation weighting factors;

---

[17] Note that we have deliberately avoided using the $D_{RS}$ classification symbol to minimize the complexity of the equations.
[18] In the absence of instrumental or environmental artifacts $\tau_c$ and $\tau_c^\ell$ should be governed by Eq. $(A1)$ for a given POI (i.e.
assuming $S_c$ doesn't change during that POI). Accordingly;
$$\log \tau_c^\ell = \log \tau_c + \log \frac{S_c^p}{S_c} = \log \tau_c + b_0$$
which is the analogue of Eq. $(A2a)$ with a = 1. Inserting this expression into equation (A1) yields $S_c = S_c^p 10^{-b_0}$. Accordingly,
in the absence of instrumental or environmental artifacts, an (Eq. (A2a)) regression slope of, $a \to 1$ and $R_{log} \to 1$ should yield
better estimates of $S_c$.

see, for example, Taylor, 1997). The weighted means and standard deviation over a given $D_{RS}$ event would be then computed as;

$$\langle S_c \rangle_\omega = \frac{\sum \omega S_c}{\sum \omega} \tag{A4a}$$

$$\sigma_\omega(S_c) = \sqrt{\frac{\sum \omega \Delta S_{c,\omega}^2}{\sum \omega}} \tag{A4b}$$

where we define $\Delta S_{c,\omega} = S_c - \langle S_c \rangle_\omega$. The $1/(\Delta S_{c,r})^2$ weighting can produce excessively non-linear weights for single measurements very near the $(\tau_c, \tau_c^\ell)$ regression line. However, their impact is considerably dampened out because we average over the POIs and then average those averages over the month.

**Appendix A2. Processing-related notes of AERONET AODs**

**A2.1 SDA and SDA$^+$ retrievals:**

The SDA and SDA$^+$ retrievals are defined in O'Neill et al. (2003) and O'Neill et al. (2008), respectively. The SDA$^+$ input wavelengths are 380 nm, 440 nm, 500 nm, 675 nm, 870 nm, 1020 nm, and 1640 nm. For the purposes of comparing AERONET data with the KLRS Doppler lidar, the SDA$^+$ output wavelength was taken as 1548 nm.

**A2.2 Backscatter Coefficient (β$_c$) profiles:**

The lidar profiles begin at a nominal altitude of 13 m. The minimum reliable measured range is <100 m (typically 75 m) (Newsom & Krishnamurthy, 2020). Our investigation into the KLRS lidar measurements shows that column measurements <51 m often appear to be artifactual (abnormally large and discontinuous $\beta_c T^2$ values as in the case of May 1). Hence, we chose to assign NaN to $\beta_c T^2$ values in this altitude range (notably to eliminate their contribution to $\tau_{dust}^\ell$).

**Appendix A3. Measurements bins and intersample times: (i) native and (ii) common-bin configuration**

To match the measurement times of all the ground-based CIMEL, lidar and OPS instruments at the KLRS site, we employed the nominal CIMEL times (i.e. the centers of the 1$^m$ CIMEL triplet bins) to generate a linear interpolation of lidar optical depths at their nominal times (the center of their 11 second time bins) and of OPS CM volume densities at their nominal times (center of their 1 minute time bins) to the nominal CIMEL times.

**A3.1 CIMEL timing protocols**

The CIMEL timing protocols, which are the basis for the $\tau_c$ time bins (actually any AERONET AOD time bin to be precise) can be found in Giles et al. (2019). Accordingly, a triplet AERONET measurement is performed every 3 minutes to separate homogeneously dispersed aerosols from highly temporally variable clouds. This is effected through a filtering process that measures triplet variability. As stated by Giles et al. (2019), a triplet is a "*series of measurements of all filters starting at 0 s*

*of the minute for a duration of about 8 s, and then repeating this measurement sequence at 30 s and 60 s from the initial measurement time. The resulting 1 min averaged measurement* [1 min average of the digital number for each filter of the 3 sets of the 8 s measurements] *sequence is defined as a triplet measurement and the maximum to minimum range of these measurements* [between individual filter measurements of the 8 s sets] *is termed the triplet variability… . The triplet*
595 *measurements are performed …. every 3 min for newer …. CE318-T instruments …. ."*

## 7 Author contribution

**Seyed Ali Sayedain:** Writing − original draft preparation – review & editing, Visualization, Investigation, Conceptualization, Methodology, Formal analysis, Data curation, Validation, Software. **Norm T. O'Neill:** Writing − review & editing, Supervision, Visualization, Conceptualization, Methodology, Formal analysis, Data curation, Validation, Funding acquisition,
600 Resources. **James King:** Writing − review & editing, Supervision, Data curation, Funding acquisition, Resources. **Patrick L. Hayes:** Writing − review & editing, Data curation, Resources. **Daniel Bellamy:** Writing − review & editing, Data curation, Validation. **Richard Washington:** Writing − review & editing, Data curation, Resources. **Sebastian Engelstaedter:** Writing − review & editing, Data curation, Resources. **Andy Vicente-Luis:** Writing − review & editing, Validation. **Jill Bachelder:** Validation. **Malo Bernhard:** Validation.

## 8 Competing interests
605

The authors declare that they have no conflict of interest.

## 9 Acknowledgements

Financial support was provided by the Canadian Mountain Network (CMN) and the Discovery Grant program of the Canadian National Sciences and Engineering Research Council (NSERC). Valuable in-kind support was provided respectively
610 by the AEROCAN network of Environment and Climate Change Canada (ECCC) and the NASA AERONET network. Valuable AERONET processing advice was provided by Tom Eck and Sasha Smirnov of the AERONET team.

## 10 Acronym and symbol glossary

In this glossary we employ, for the sake of simplicity, an argument of "$(z)$" to represent "$(0, z)$" for transmission ($T$) expressions and no argument for optical depth parameters when their columnar extent is made evident by their subscript

| | |
|---|---|
| AEROCAN | Canadian subnetwork of AERONET |
| AERONET | Aerosol Robotic Network of CIMEL sunphotometer / sky radiometers |

| | |
|---|---|
| $\beta'(z)$ | Attenuated backscatter coefficient ($\beta(z)\,T_c^2(z)$ with units of km$^{-1}$ sr$^{-1}$) |
| AOD | Aerosol Optical Depth (unitless) |
| $\beta'(z)$ | Attenuated backscatter coefficient ($\beta(z)\,T_c^2(z)$ with units of km$^{-1}$ sr$^{-1}$) |
| $\beta_c(z)$ | Coarse mode backscatter coefficient (units of km$^{-1}$ sr$^{-1}$) |
| $\beta'_c(z)$ | Coarse mode attenuated backscatter coefficient ($\beta_c(z)\,T_c^2(z)$ with units of km$^{-1}$ sr$^{-1}$) |
| $\beta_{c,\sim}(z)$ | $\beta_c$ approximation given by equation (2) |
| CM | Coarse Mode |
| $D$ | Classification symbol for optically significant Dust event |
| $D_{FPC}$ | Classification acronym for an FPC event |
| $D_{GEN}$ | Classification acronym for generic dust subclass |
| $D_{NRS}$ | Classification acronym for optically significant Dust that cannot be remotely sensed |
| $D_{RS}$ | Classification acronym for optically significant Dust that can be remotely sensed |
| DLH | Dust layer height |
| DV | Down valley |
| $dv/dlogD$ | Particle-volume distribution (µm$^3$µm$^{-3}$ per unit increment in log diameter). This PSD is derived from the particle number PSD output of the OPS instruments ($dn/dlogD$ where $dn$ is the particle number in a given size bin) |
| $dv/dlnr$ | Particle-volume distribution (µm$^3$µm$^{-3}$ per unit increment in log r) |
| $dV/dlnr$ | Columnar particle-volume per unit area in the differential bin dlogr (AERONET product with units of µm$^3$µm$^{-2}$) |
| FPC | Classification symbol for a False Positive Cloud event |
| FM | Fine Mode |
| HLD | High Latitude Dust |
| KLRS | Kluane Lake (Lhù'ààn Mân') Research Site |
| LCH | Lidar Ceiling Height (9.6 km) |
| MCA | Minimum cloud altitude (units of km) |
| NaN | Not a number |
| OPC | Optical Particle Counter (from which $v_{dust}(0)$ is determined) |
| OPS | Optical Particle Sizer (from which $v_{dust}(0)$ is determined) |
| POI | Period of Interest |
| PSD | Particle Size Distribution |
| $r$ | Radius (µm) |
| $R_{log}$ | Correlation coefficient in log-log space ($\log \tau_c^\ell$ vs $\log \tau_c$ for example) |

| SDA | Spectral Deconvolution Algorithm |
|---|---|
| $S_c$ | AERONET derived lidar ratio |
| $S_c^p$ | Prescribed Lidar Ratio computed from Mie calculation |
| $S_{c,reg}$ | AERONET derived lidar ratio where we force a given data pair, $\left(\tau_c, \tau_{dust}^\ell\right)$ to lie on the regression line (subclass $D_{RS}$ data pairs: the "c" subscript is used to simplify the nomenclature) |
| $\sigma(x)$ | Arithmetic standard deviation of the parameter x |
| $T_c(z)$ | Altitude dependent (one-way) transmission of a lidar pulse |
| $T_{c,\sim}(z)$ | $T_c(z)$ approximation obtained by employing the ratio $\tau_{\beta_c'}(0,z)/\tau_{\beta_c'}$ as the altitude defining profile of $\tau_c(0,z)$ |
| $\tau_{\beta_c}$ | Column-integrated CM backscatter coefficient (coarse mode backscatter optical depth) |
| $\tau_{\beta_c'}$ | Column-integrated CM attenuated backscatter coefficient (CM attenuated backscatter optical depth) |
| $\tau_c$ | CM AOD at 1548 nm (AERONET SDA+ product) |
| $\tau_{c,inv}$ | CM inversion AOD at 1548 nm (AERONET interpolated-inversion product) |
| $\tau_c^\ell$ | CM lidar AOD at 1548 nm with integrating range of $0 - LCH$ |
| $\tau_{D,reg}^\ell$ | CM lidar AOD at 1548 nm where we force a given data pair, $\left(\tau_c, \tau_D^\ell\right)$ to lie on the regression line |
| $\tau_{dust}^\ell$ | CM lidar AOD at 1548 nm with integrating range of $0-DLH$ ( $\tau_c^\ell(0, DLH)$ ) |
| $\tau_D^\ell$ | Sequence of $\tau_{dust}^\ell$ values that are promoted to a class D POI |
| $\tau_{cloud}^\ell$ | CM lidar AOD at 1548 nm with integrating range of $DLH-LCH$ (cloud region) |
| $U$ | Classification acronym for events that failed to achieve a $D$ classification |
| $v_{dust}(0)$ | Surface (z = 0) CM OPS particle-volume concentration at KLRS (units of $\mu m^3 \mu m^{-3}$) . The CM OPS integration was computed over 9 bins whose bin-center radii ranged from 0.78 to 4.51 µm |
| $V_c$ | AERONET-derived, CM columnar particle-volume concentration (units of $\mu m^3 \mu m^{-2}$). The CM integration of the $dV/dlnr$ retrieval is computed from the bin containing the $dV/dlnr$ minimum (that dynamic minimum being constrained to a bin-center radius range from 0.439 to 0.992 µm) to the largest retrieval bin (15 µm bin-center radius) |
| $\langle x \rangle$ | Arithmetic mean of the parameter x |
| $z$ | Altitude above ground level (units of km) |

615 **References**

AboEl-Fetouh, Y., O'Neill, N. T., Ranjbar, K., Hesaraki, S., Abboud, I., and Sobolewski, P. S.: Climatological-Scale Analysis of Intensive and Semi-intensive Aerosol Parameters Derived From AERONET Retrievals Over the Arctic, Journal of Geophysical Research: Atmospheres, 125(10), doi:10.1029/2019jd031569, 2020.

Bachelder, J., Cadieux, M., Liu-Kang, C., Lambert, P., Filoche, A., Galhardi, J. A., Hadioui, M., Chaput, A., Bastien-
620 Thibault, M. P., Wilkinson, K. J., King, J., & Hayes, P. L.: Chemical and microphysical properties of wind-blown dust near

an actively retreating glacier in Yukon, Canada, Aerosol Science and Technology, 54(1), 2–20, doi: 10.1080/02786826.2019.1676394, 2020.

Baldo, C., Formenti, P., Nowak, S., Chevaillier, S., Cazaunau, M., Pangui, E., Di Biagio, C., Doussin, J. F., Ignatyev, K., Dagsson-Waldhauserova, P., Arnalds, O., Mackenzie, A. R., & Shi, Z.: Distinct chemical and mineralogical composition of
625 Icelandic dust compared to northern African and Asian dust. Atmospheric Chemistry and Physics, 20(21), 13521–13539, doi:10.5194/acp-20-13521-2020, 2020.

Bullard, J. E., Matthew, B., Tom, B., John, C., Eleanor, D., Diego, G., Santiago, G., Gudrun, G., Richard, H., Robert, M., Cheryl, M.-N., Tom, M., Helena, S., & Thorsteinsson, T.: High latitude dust in the Earth system Reviews of Geophysics, Reviews of Geophysics, 54, 447–485, doi:10.1002/2016RG000518, 2016.

630 Chiang, C.-W., Nee, J.-B., & Chen, W.-N.: Lidar ratio and depolarization ratio for cirrus clouds, Applied Optics, Vol. 41, Issue 30, Pp. 6470-6476, 41(30), 6470–6476, doi:10.1364/AO.41.006470, 2002.

Cottle, P., Strawbridge, K., Mckendry, I., O'Neill, N., & Saha, A.: A pervasive and persistent Asian dust event over North America during spring 2010: Lidar and sunphotometer observations, Atmospheric Chemistry and Physics, 13(9), 4515–4527, doi:10.5194/acp-13-4515-2013, 2013.

635 Crusius, J., Schroth, A. W., Gassó, S., Moy, C. M., Levy, R. C., & Gatica, M.: Glacial flour dust storms in the Gulf of Alaska: Hydrologic and meteorological controls and their importance as a source of bioavailable iron, Geophysical Research Letters, 38(6), 1–5, doi:10.1029/2010GL046573, 2011.

Dagsson-Waldhauserova, P., Renard, J. B., Olafsson, H., Vignelles, D., Berthet, G., Verdier, N., & Duverger, V.: Vertical distribution of aerosols in dust storms during the Arctic winter, Scientific Reports, 9(1), 1–11, doi:10.1038/s41598-019-51764-
640 y, 2019.

Dörnbrack, A., Stachlewska, I. S., Ritter, C., & Neuber, R.: Aerosol distribution around Svalbard during intense easterly winds, Atmospheric Chemistry and Physics, 10(4), 1473–1490, doi:10.5194/ACP-10-1473-2010, 2010.

Dubovik, O., & King, M. D.: A flexible inversion algorithm for retrieval of aerosol optical properties from Sun and sky radiance measurements, Journal of Geophysical Research Atmospheres, 105(D16), 20673–20696,
645 doi:10.1029/2000JD900282, 2000.

Esselborn, M., Wirth, M., Fix, A., Weinzierl, B., Rasp, K., Tesche, M., & Petzold, A.: Spatial distribution and optical properties of Saharan dust observed by airborne high spectral resolution lidar during SAMUM 2006. Tellus, Series B: Chemical and Physical Meteorology, 61(1), 131–143, https://doi.org/10.1111/j.1600-0889.2008.00394.x, 2009.

Evan, A., Walkowiak, B., & Frouin, R.: On the Misclassification of Dust as Cloud at an AERONET site in the Sonoran
650 Desert, Journal of Atmospheric and Oceanic Technology, 1(aop), doi:10.1175/JTECH-D-21-0114.1, 2021.

Evans, B., personal communication, 1994.

Formenti, P., Caquineau, S., Desboeufs, K., Klaver, A., Chevaillier, S., Journet, E., and Rajot, J. L.: Mapping the physicochemical properties of mineral dust in western Africa: mineralogical composition, Atmos. Chem. Phys., 14, 10663–10686, https://doi.org/10.5194/acp-14-10663-2014, 2014.

Giles, D. M., Sinyuk, A., Sorokin, M. G., Schafer, J. S., Smirnov, A., Slutsker, I., Eck, T. F., Holben, B. N., Lewis, J. R., Campbell, J. R., Welton, E. J., Korkin, S. V., & Lyapustin, A. I.: Advancements in the Aerosol Robotic Network (AERONET) Version 3 database - Automated near-real-time quality control algorithm with improved cloud screening for Sun photometer aerosol optical depth (AOD) measurements, Atmospheric Measurement Techniques, 12(1), 169–209, doi:10.5194/amt-12-169-2019, 2019.

Groot Zwaaftink, C. D., Grythe, H., Skov, H., & Stohl, A.: Substantial contribution of northern high-latitude sources to mineral dust in the Arctic, Journal of Geophysical Research, 121(22), 13,678-13,697, doi:10.1002/2016JD025482, 2016.

Hesaraki, S., O'Neill, N. T., Lesins, G., Saha, A., Martin, R. V., Fioletov, V. E., Baibakov, K., & Abboud, I.: Comparisons of a Chemical Transport Model with a Four-Year (April to September) Analysis of Fine- and Coarse-Mode Aerosol Optical Depth Retrievals Over the Canadian Arctic, Atmosphere - Ocean, 55(4–5), 213–229, doi:10.1080/07055900.2017.1356263, 2017.

Hansen, J.E., Travis, L.D.: Light scattering in planetary atmospheres, *Space Sci Rev* **16**, 527–610, https://doi.org/10.1007/BF00168069, 1974.

Holben, B. N., Eck, T. F., Slutsker, I., Tanré, D., Buis, J. P., Setzer, A., Vermote, E., Reagan, J. A., Kaufman, Y. J., Nakajima, T., Lavenu, F., Jankowiak, I., & Smirnov, A.: AERONET - A federated instrument network and data archive for aerosol characterization, Remote Sensing of Environment, 66(1), 1–16, https://doi.org/10.1016/S0034-4257(98)00031-5, 1998.

Huck, R. A., Bryant, R. G., and King, J.: The importance of detection thresholds for the quantification of source and timing of high-latitude dust emission using remote sensing, EGUsphere [preprint], https://doi.org/10.5194/egusphere-2022-1156, 2023.

King, J.: X-ray Diffraction determined mineralogy and complex refractive indices of PM10 from the A'ay Chu. Unpublished manuscript, 2023.

Meinander, O., Dagsson-Waldhauserova, P., Amosov, P., Aseyeva, E., Atkins, C., Baklanov, A., Baldo, C., Barr, S. L., Barzycka, B., Benning, L. G., Cvetkovic, B., Enchilik, P., Frolov, D., Gassó, S., Kandler, K., Kasimov, N., Kavan, J., King, J., Koroleva, T., Krupskaya, V., Kulmala, M., Kusiak, M., Lappalainen, H. K., Laska, M., Lasne, J., Lewandowski, M., Luks, B., McQuaid, J. B., Moroni, B., Murray, B., Möhler, O., Nawrot, A., Nickovic, S., O'Neill, N. T., Pejanovic, G., Popovicheva, O., Ranjbar, K., Romanias, M., Samonova, O., Sanchex-Marroquin, A., Schepanski, K., Semenkov, I., Sharapova, A., Shevnina, E., Shi, Z., Sofiev, M., Thevenet, F., Thorsteinsson, T., Timofeev, M., Silas Umo, N., Uppstu, A., Urupina, D., Varga, G., Werner, T., Arnalds, O., Vukovic Vimic, A.: Newly identified climatically and environmentally significant high-

latitude dust sources. Atmospheric Chemistry and Physics, 22(17), 11889–11930, https://doi.org/10.5194/acp-22-11889-2022, 2022.

Newsom, R., & Krishnamurthy, R.: Doppler Lidar (DL) Instrument Handbook, doi:10.2172/1034640, 2020.

Nickling, W. G.: Eolian Sediment Transport During Dust Storms: Slims River Valley, Yukon Territory, Can J Earth Sci, 15(7), 1069–1084, doi:10.1139/e78-114, 1978.

O'Neill, N. T., Eck, T. F., Reid, J. S., Smirnov, A., & Pancrati, O.: Coarse mode optical information retrievable using ultraviolet to short-wave infrared Sun photometry: Application to United Arab Emirates Unified Aerosol Experiment data, Journal of Geophysical Research Atmospheres, 113(5), 1–11, doi:10.1029/2007JD009052, 2008.

O'Neill, N. T., Eck, T. F., Smirnov, A., Holben, B. N., & Thulasiraman, S.: Spectral discrimination of coarse and fine mode optical depth, Journal of Geophysical Research D: Atmospheres, 108(17), 1–15, doi:10.1029/2002jd002975, 2003.

O'Neill, N. T., Ignatov, A., Holben, B. N., & Eck, T. F.: The lognormal distribution as a reference for reporting aerosol optical depth statistics; Empirical tests using multi-year, multi-site AERONET sunphotometer data, Geophysical Research Letters, 27(20), 3333–3336, doi:10.1029/2000GL011581, 2000.

Pearson, G., Davies, F., & Collier, C.: An analysis of the performance of the UFAM pulsed Doppler lidar for observing the boundary layer, Journal of Atmospheric and Oceanic Technology, 26(2), 240–250, doi:10.1175/2008JTECHA1128.1, 2009.

Ranjbar, K., O'Neill, N. T., Ivanescu, L., King, J., & Hayes, P. L.: Remote sensing of a high-Arctic, local dust event over Lake Hazen (Ellesmere Island, Nunavut, Canada), Atmospheric Environment, 246, 118102, https://doi.org/10.1016/j.atmosenv.2020.118102, 2021.

Sayer, A. M., & Knobelspiesse, K. D.: How should we aggregate data? Methods accounting for the numerical distributions, with an assessment of aerosol optical depth, Atmos. Chem. Phys, 19, 15023–15048, doi:10.5194/acp-19-15023-2019, 2019.

Shugar, D. H., Clague, J. J., Best, J. L., Schoof, C., Willis, M. J., Copland, L., & Roe, G. H.: River piracy and drainage basin reorganization led by climate-driven glacier retreat, Nature Geoscience, 10(5), 370–375, doi:10.1038/ngeo2932, 2017.

Sinyuk, A., Holben, B. N., Eck, T. F., Giles, D. M., Slutsker, I., Korkin, S., Schafer, J. S., Smirnov, A., Sorokin, M., & Lyapustin, A.: The AERONET Version 3 aerosol retrieval algorithm, associated uncertainties and comparisons to Version 2, Atmos. Meas. Tech, 13, 3375–3411, doi:10.5194/amt-13-3375-2020, 2020.

Sokolik, I. N., & Toon, O. B.: Incorporation of mineralogical composition into models of the radiative properties of mineral aerosol from UV to IR wavelengths, Journal of Geophysical Research Atmospheres, 104(D8), 9423–9444, doi:10.1029/1998JD200048, 1999.

Taylor, J. R.: An introduction to error analysis : the study of uncertainties in physical measurements, University Science Books, 327pp., 1997.

715  Weinzierl, B., Petzold, A., Esselborn, M., Wirth, M., Rasp, K., Kandler, K., Schütz, L., Koepke, P., & Fiebig, M.: Airborne measurements of dust layer properties, particle size distribution and mixing state of Saharan dust during SAMUM 2006. Tellus, Series B: Chemical and Physical Meteorology, 61(1), 96–117, https://doi.org/10.1111/j.1600-0889.2008.00392.x, 2009.

Weitkamp, C.: Lidar : range-resolved optical remote sensing of the atmosphere, In Springer series in optical sciences, (Issue 102), doi:10.1007/b106786, 2005.